

RESEARCH ARTICLE

10.1029/2017JF004280

Key Points:

- Seismic refraction, drilling, and geostatistics provide insight into deep critical zone structure at unprecedented scales
- Multiple processes conspire to influence variations in subsurface fracturing and weathering
- Variability in saprolite and fractured bedrock thickness is not readily explained by models of critical zone evolution

Supporting Information:

- Supporting Information S1

Correspondence to:

B. A. Flinchum,
brady.flinchum@csiro.au

Citation:

Flinchum, B. A., Steven Holbrook, W., Rempe, D., Moon, S., Riebe, C. S., Carr, B. J., et al. (2018). Critical zone structure under a granite ridge inferred from drilling and three-dimensional seismic refraction data. *Journal of Geophysical Research: Earth Surface*, 123, 1317–1343. <https://doi.org/10.1029/2017JF004280>

Received 6 MAR 2017

Accepted 7 MAY 2018

Accepted article online 18 MAY 2018

Published online 16 JUN 2018

Critical Zone Structure Under a Granite Ridge Inferred From Drilling and Three-Dimensional Seismic Refraction Data

Brady A. Flinchum^{1,2,3} , W. Steven Holbrook^{1,2} , Daniella Rempe⁴ , Seulgi Moon⁵ , Clifford S. Riebe^{1,2} , Bradley J. Carr^{1,2} , Jordan L. Hayes^{1,2,6} , James St. Clair^{1,2,7}, and Marc Philipp Peters^{1,2}

¹Department of Geology and Geophysics, University of Wyoming, Laramie, WY, USA, ²Wyoming Center for Environmental Hydrology and Geophysics, University of Wyoming, Laramie, WY, USA, ³CSIRO Land and Water, PMB 2, Glen Osmond, South Australia, Australia, ⁴Jackson School of Geosciences, University of Texas at Austin, Austin, TX, USA, ⁵Earth, Planetary, and Space Sciences, University of California Los Angeles, Los Angeles, CA, USA, ⁶Department of Earth Sciences, Dickinson College, Carlisle, PA, USA, ⁷Idaho National Laboratory, Idaho Falls, ID, USA

Abstract Observing the critical zone (CZ) below the top few meters of readily excavated soil is challenging yet crucial to understanding Earth surface processes. Near-surface geophysical methods can overcome this challenge by imaging the CZ in three dimensions (3-D) over hundreds of meters, thus revealing lateral heterogeneity in subsurface properties across scales relevant to understanding hillslope erosion, weathering, and biogeochemical cycling. We imaged the CZ under a soil-mantled ridge developed in granitic terrain of the Laramie Range, Wyoming, using data from five boreholes and a 3-D volume (970 by 600 by 80 m) of seismic velocities generated by ordinary kriging of 25 two-dimensional seismic refraction transects. The observed CZ structure under the ridge broadly matches predictions of two recently proposed hypotheses: the uppermost surface of weathered bedrock is consistent with subsurface weathering driven by bedrock drainage and subsurface topography defining the top of unweathered protolith is consistent with fracturing predicted from topographic and regional stresses. In contrast, differences in slope aspect along the ridge are too subtle to explain observed variations in regolith structure. Our observations suggest that multiple processes, each of which may dominate at different depths, work in concert to regulate deep CZ structure.

1. Introduction

The conversion of bedrock to soil is driven by diverse chemical, biological, and physical processes within a spatially variable and complex zone spanning the top 10 to 100 m of Earth's subsurface (Riebe et al., 2017). This so-called critical zone (CZ) has been the focus of increasingly cross-disciplinary studies within the growing international network of critical zone observatories in the United States, Europe, and China (White et al., 2015). Soil, the mobile weathering product of bedrock on mountain slopes, supports ecosystems and agriculture (Heimsath et al., 2012; Montgomery, 2007), influences local hydrology (Bales et al., 2011), sustains biogeochemical cycles (Chorover et al., 2007), and can be eroded and redistributed to shape landscapes (Allen, 2008). The structure of the CZ influences surface-groundwater interactions (Jencso et al., 2010; Katsuyama et al., 2010; Kollet & Maxwell, 2008; Montgomery et al., 1997; Voltz et al., 2013), solute transport (Holloway et al., 1998; Kuntz et al., 2011; Singha et al., 2011), the distribution of plant-available water (Brooks et al., 2010; Graham et al., 2010; McDonnell, 2014), and the downstream delivery of water to humans and ecosystems (Andermann et al., 2012; Hood et al., 2006; Lowry et al., 2007). Characterizing CZ structure and understanding the processes that shape it are therefore central to a comprehensive understanding of hydrology, biogeochemical cycling, weathering, and erosion in mountain landscapes.

The CZ can be highly variable in both thickness and structure due to aboveground variations in vegetation (Hahm et al., 2014) and slope aspect (Anderson et al., 2013; Rempel et al., 2016), as well as subsurface gradients in weathering (Lebedeva & Brantley, 2013), hydrologic properties (Rempe & Dietrich, 2014), and topographic stress fields (Slim et al., 2014; St. Clair et al., 2015). Quantifying variability in CZ architecture and identifying the processes that created it are challenging because the deep CZ is difficult to access and study over relevant scales (Riebe et al., 2017). Boreholes can provide a detailed one-dimensional (1-D) view of the deep CZ, and cores extracted from them can be used to directly quantify downhole variations in geochemical and geophysical properties (e.g., Anderson et al., 2002; Bazilevskaia et al., 2013; Buss et al., 2013; White et al., 1998). However, because the CZ is highly variable, a single borehole from just one point at the surface may

not be representative of the surrounding landscape. Moreover, drilling many holes can be prohibitively expensive and logistically challenging, particularly in mountainous landscapes where CZ studies are often focused. Road cuts can provide a more representative two-dimensional (2-D) perspective, but their happenstance distribution is unlikely to reveal a complete view of how deep CZ structure varies across the landscape.

In contrast, geophysical measurements can be gathered in focused surveys designed to systematically and noninvasively explore the deep CZ over broad spatial scales (e.g., Parsekian et al., 2015; Robinson et al., 2008). CZ researchers have increasingly used them to document lateral and vertical variability in regolith properties (Befus et al., 2011; Holbrook et al., 2014; Leopold et al., 2008, 2013; Olona et al., 2010; Orlando et al., 2016), to estimate bedrock fracture density (Clarke & Burbank, 2011; Heincke et al., 2006), to determine shallow aquifer structure (Garambois et al., 2002; Gburek et al., 1999; Gburek & Urban, 1990; McClymont et al., 2011; Pasquet et al., 2015), to constrain depth to bedrock (Mills, 1990; Nyquist et al., 1996; Pavich, 1986), and to explore the relationship between topographic stress and fracture density (St. Clair et al., 2015). One drawback is that indirect measurements from geophysical tools can be ambiguous about variations in subsurface properties unless boreholes are drilled along the survey lines for calibration through direct observations. Moreover, geophysical studies of the deep CZ are a relatively new addition to the growing field of CZ science (Parsekian et al., 2015). Thus, although many studies have focused on understanding the production, erosion, and biogeochemical cycling of soil in the top several meters of the CZ, relatively few have explored the deep CZ and the processes that regulate its architecture (e.g., Riebe et al., 2017).

Because so few geophysical studies have been conducted, little is known about how CZ structure varies as a function of landscape position (i.e., from ridge top to valley bottom), bedrock geology, and ambient climate—especially over landscape scales. CZ structure has been variously conceptualized as a four-layer system of protolith, fractured bedrock, saprolite, and soil (Anderson et al., 2007, 2012; Befus et al., 2011; Graham et al., 1997; Holbrook et al., 2014; Pavich, 1986), as a three-layer system of protolith, saprolite, and soil (Dixon et al., 2009; Dixon & Riebe, 2014; Riebe & Granger, 2013), as a simpler two-layer system of weathered and unweathered material (Lebedeva & Brantley, 2013; Rempe & Dietrich, 2014), and as a less stratified matrix of core stones decreasing in size from protolith to soil (Acworth, 1987; Brantley et al., 2011; Buss et al., 2013; Fletcher & Brantley, 2010; Graham et al., 2010). The lack of consensus about how to subdivide the CZ in part reflects the lack of data on the following: the vertical and horizontal extent of subsurface layers, whether or not the transitions between layers are gradational or sharp, and even which layers exist in different landscapes. The fact that individual layers may exist in some landscapes but not in others suggests that it may not be possible to develop a universal model of regolith formation.

Although observations of CZ structure are rare, even less is known about the processes that create and regulate it. However, a series of testable theoretical models have recently been developed (see Riebe et al., 2017 for a review). These include weathering front advance into protolith at depth due to vertical throughflow of reactive fluids from the surface (Lebedeva et al., 2007, 2010; Lebedeva & Brantley, 2013; Lichtner, 1988; Maher, 2010; Maher & Chamberlain, 2014; Steefel et al., 2005), chemical weathering due to lateral flow at the bedrock-weathered rock interface (Braun et al., 2016), fracturing of unweathered bedrock due to subsurface gradients in topographic and regional stresses (Slim et al., 2014; St. Clair et al., 2015), climatic forcing of weathering front advance via environmental energy and mass transfer (e.g., Chorover et al., 2011), bedrock damage due to frost cracking (Anderson et al., 2013; Rempel et al., 2016), bedrock disruption and weathering by biological processes (Brantley, Eissenstat, et al., 2017; Pawlik et al., 2016; Roering et al., 2010), and weathering advance due to drainage of chemically equilibrated fluids from bedrock pore spaces (Rempe & Dietrich, 2014). These models, which feature different chemical, hydrological, and physical processes, lead to diverse predictions about the thickness of layers within the CZ and the shape of surfaces that form their interfaces (Riebe et al., 2017). In practice, multiple processes probably conspire to influence CZ structure, but there is little data to test this hypothesis in mountain landscapes. As a result, the relative importance of the CZ processes outlined above remains largely unknown.

Here we present a new 3-D data set on subsurface weathering along a ridge underlain by granite bedrock in the Laramie Range, Wyoming. We built this data set by kriging extensive, crosscutting 2-D geophysical surveys and calibrating the results with observations from five boreholes. The resulting ~ 45 million m^3 image of weathered rock and saprolite provides an unprecedented 3-D perspective on subsurface weathering in a mountain setting. This allows us to test for consistency with prevailing hypotheses about processes that

regulate CZ structure under the landscape surface. We use the data to define two key surfaces at depth: the interface between saprolite and weathered bedrock and the interface between weathered rock and protolith. Our observations reveal subsurface complexity and heterogeneity that cannot be explained by a single process. However, our analysis suggests that deep CZ structure is regulated by a combination of (1) fracturing due to topographic stresses, which controls the elevation of the interface between protolith and weathered bedrock, and (2) weathering following drainage of bedrock pore fluids, which controls the elevation of the interface between weathered bedrock and saprolite.

2. Geologic Setting

The Blair Wallis (BW) study site lies within the U.S. Forest Service land approximately 21 km southeast of the city Laramie in the Laramie Range, Wyoming. Over the past 5 years, the site has become one of two main study areas for the Wyoming Center for Environmental Hydrology and Geophysics (WyCEHG; Carey & Paige, 2016; Hayes, 2016). It provides an excellent opportunity to study deep CZ architecture in nonglaciated granitic terrain that is undisturbed by human land use. Moreover, we were able to capitalize on extensive existing information about the site in analyses presented here.

The BW site is part of the Rocky Mountain surface (Bradley, 1987; Chapin & Kelley, 1997; Egger et al., 1969; Evanoff, 1990), which is defined by gentle undulating topography (Figure 1a) that is distinct from the sharp peaks of the Front Range. Although this surface is thought to have origins in the Eocene (Gregory & Chase, 1994; Mears, 1993; Moore, 1960; Scott & Taylor, 1986), regional studies of cosmogenic nuclides (e.g., Dethier et al., 2014) indicate that erosion has been lowering the surface (Bradley, 1987; Egger et al., 1969) at a rate sufficient to replace the local relief every 1 to 2 million years.

To obtain a locally representative view of the 3-D CZ structure in the region, we focused on a ridge lying in gently undulating topography that is typical of the surrounding region (Figure 1a). The ridge is similar in relief and aspect to the surrounding terrain to the northwest, west, and south of our study site, so our analysis should be broadly representative of regional CZ architecture (Figure 1a). Relief along the ridge is 15 m on average. The valleys on either side are separated by approximately 260 m at the western edge of the study area and converge to the east as the ridge dives at a slope of $\sim 3^\circ$ toward the valley confluence (Figure 1b). The contributing area of the northern valley is too small to support a channel, whereas the 4.2-km² catchment area of the southern valley supports a small perennial stream, which might explain why the two valleys are asymmetrical. Not surprisingly, given the low-relief and crystalline bedrock of the region, cosmogenic nuclide studies of alluvium and bedrock nearby (including a data point from ~ 6 km northeast of our site) have shown that erosion rates are just 20–40 mm/kyr (Dethier et al., 2014), reflecting a slow pace of change in the CZ over the $\sim 20,000$ -year timescales averaged by the cosmogenic approaches.

Ten years of local climate data from the Crow Creek SNOTEL station show that the BW site has a mean annual temperature of 5.4 °C and receives 620 mm of annual precipitation, with 90% falling as snow (Natural Resources Conservation Service (NRCS), 2015). Average temperature in the summer (June to September) is approximately 15 °C, and average temperature in the winter (December to March) is approximately -5 °C. Mammalian fossils from nearby (~ 150 km) indicate that the late glacial and postglacial climate was at least 3.5 °C cooler than present day (Roberts, 1970). The stream hydrograph peaks between April and June due to snowmelt. The dominant vegetation along our study ridge is sagebrush (*Artemisia tridentate ssp. spiciformis*). In the low-lying areas, especially near surface water, aspen (*Populus tremuloides*), lodgepole pine (*Pinus contorta var. latifolia*), and willow (*Salix spp.*) are abundant.

The ridge lies within the Sherman Batholith, which consists of 1.4-Ga granitic rocks (Frost et al., 1999; Peterman & Hedge, 1968; Zielinski et al., 1982). The Sherman Batholith was uplifted to its present location during the Laramide Orogeny. Metamorphism has been minor since batholith emplacement (Peterman & Hedge, 1968), and although the batholith harbors geochemically diverse bedrock (Edwards & Frost, 2000), our site is developed on relatively uniform Sherman granite (Figure 1a).

Soil mapping was completed in 1998 using aerial photographs and field observations at selected locations using a truck-mounted hydraulic probe (Natural Resources Conservation Service, 1988). The NRCS reports six mapped soils within the 16-km² area outlined in Figure 1a. The maximum reported soil thickness in the area is 107 cm, the minimum thickness (excluding outcrop) is 28 cm, and the average is 65 cm. The

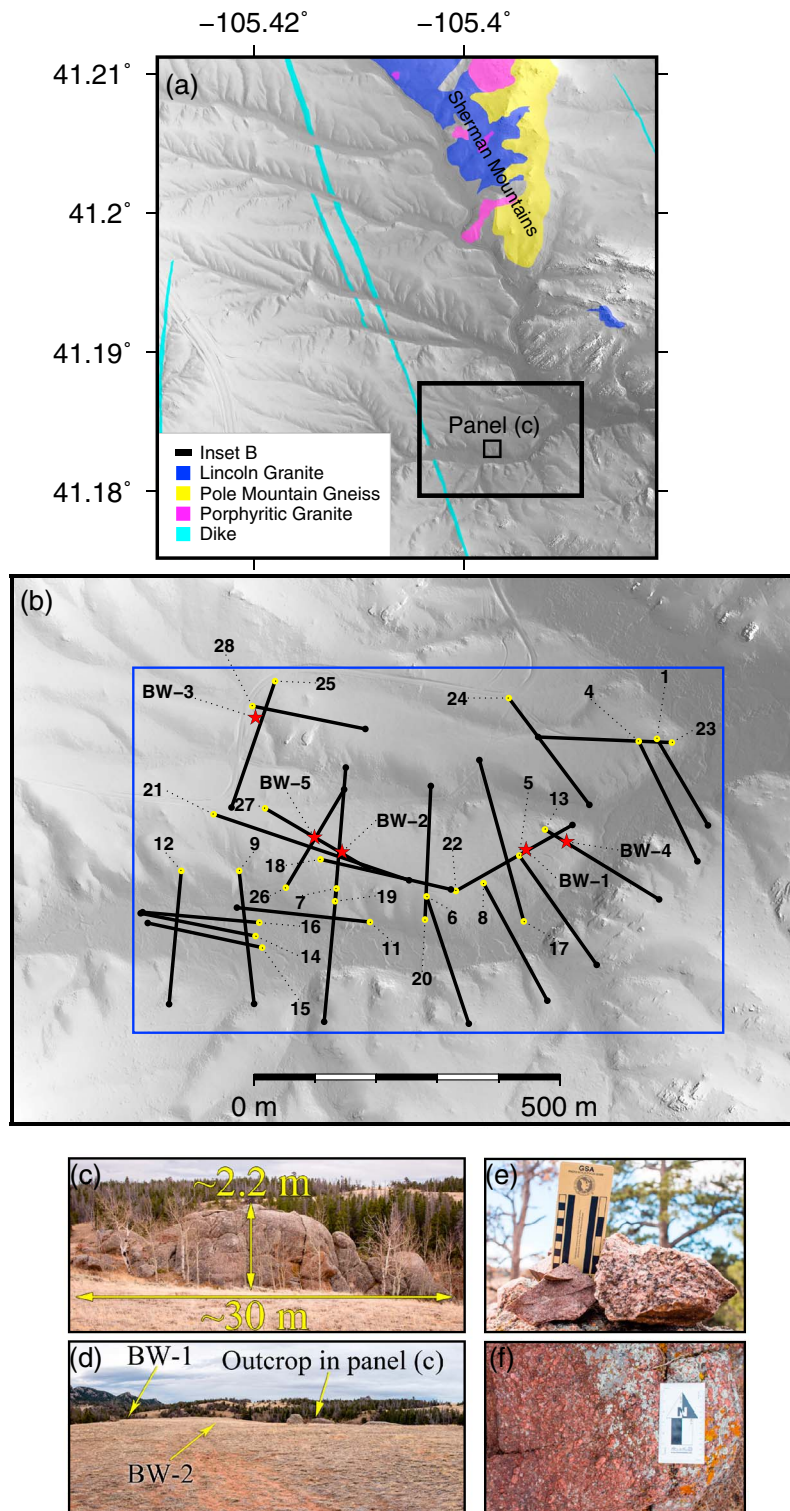


Figure 1. (a) Regional hillshade of the Laramie Range showing mapped geologic units from Ver Ploeg and McLaughlin (2010). Areas that are not colored were mapped as Sherman granite. (b) Map showing the seismic refraction transects (black lines) on light detecting and ranging (LIDAR) hillshade. Yellow circles indicate the start of each profile, and dotted lines indicate the profile number. Survey geometry of each seismic line can be found in Table 1. The blue box indicates the extent of the 3-D kriging volume, and red stars indicate borehole locations, labeled with a dotted line and the prefix “BW” (e.g., BW-1). (c) Image of an outcrop located on the southern part of the ridge (panel a), taken near the start of line 19 looking southeast. (d) Image taken standing on BW-5 looking east, which demonstrates the lack of outcrop and gentleness of the ridge. (e) Image showing the Lincoln (left sample) versus Sherman (right sample) granite. (f) Image showing the change in both color and texture of the porphyritic granite.

spatial extent and physical characteristics of the soil were digitized and archived by the NRCS (Natural Resources Conservation Service, 2017).

Although bedrock is mapped as a texturally and geochemically uniform granite along our study ridge (Ver Ploeg & McLaughlin, 2010), heterogeneities in lithology correspond to variations in topography and CZ thickness elsewhere in the region (Edwards & Frost, 2000). For example, the Pole Mountain Gneiss forms the spine of the pronounced Sherman Mountains approximately 5 km to the north (Ver Ploeg & McLaughlin, 2010) and local outcrops of Lincoln and porphyritic granite, which are chemically and texturally distinct from the more widespread Sherman granite, exist throughout the batholith (Figure 1a). Meanwhile, the Sherman (Figure 1e) underlies many of the area's gently sloping ridges including the BW study site. It is coarse grained, with 30–40% microcline, 15–30% quartz, 20% plagioclase, 10–15% perthite, 5–10% biotite, and higher concentrations of iron and potassium than the Lincoln and porphyritic granites (Edwards & Frost, 2000; Frost et al., 1999; Geist et al., 1989). The Lincoln granite (Figure 1e), in contrast, is finer grained and contains more quartz and plagioclase. It occurs in relatively small plugs scattered throughout the batholith, most notably 3 km north of our study site (Frost et al., 1999; Ver Ploeg & McLaughlin, 2010; Figure 1a). The porphyritic granite, in contrast, has large phenocrysts (Figure 1f), is darker in color than the Lincoln, and occurs as intrusions or dikes containing Sherman xenoliths and mafic enclaves. It has been argued that differences in mineralogy and bulk geochemistry across the region may help explain broad variations in topography and CZ thickness (Eggler et al., 1969). However, over the relatively small hillslope scale of our study, bedrock is geochemically homogenous enough that the spatial patterns in CZ architecture are not caused by variations in lithology. We therefore hypothesize that CZ architecture is strongly coupled to processes such as frost cracking (Anderson et al., 2013; Rempel et al., 2016), kinetically limited weathering (Lebedeva & Brantley, 2013), drainage of bedrock pore fluids (Rempe & Dietrich, 2014), and gradients in the subsurface stress field (Moon et al., 2017; Slim et al., 2014; St. Clair et al., 2015).

3. Methods

3.1. Seismic Acquisition and Modeling

The 25 seismic refraction lines (Figure 1b) in the study area were collected using 24-channel Geometrics Geode seismographs. The source was a 4.5-kg sledgehammer swung onto an aluminum plate. Shot spacing varied between 5 and 15 m (Table 1). Lines in the survey area used 48, 96, or 192 channels, and geophone spacing ranged between 1 and 4 m (Table 1). Manually picked arrival times were inverted for p wave velocity (V_p) using a traveltime tomography code written in Matlab (St. Clair, 2015). The inversion is parameterized as a sheared mesh of constant velocity parallelograms of fixed width and height that increase linearly with depth. Rays are traced through the mesh using a shortest path algorithm (Dijkstra, 1959; Moser, 1991; Moser et al., 1992), and updates are found by solving a regularized, linear inverse problem. The ray tracing and inversion steps are iterated until a satisfactory fit to the data has been achieved. To quantify uncertainty of the final velocity model to the initial starting model, we used Monte Carlo simulations (supporting information S1). The Monte Carlo simulations provide an average velocity model and standard deviation of velocity at each pixel of the mesh. The resulting tomograms likely image structures that are tens of meters in scale.

In addition to the 25 seismic refraction profiles, we collected data from a short profile 9 km north on an outcrop of intact Sherman granite with less than one fracture per meter (Figure 2a). The outcrop survey used 72 geophones spaced at 25 cm, a shot spacing of 1 m, and a 1.8-kg hammer on an aluminum plate as a source. We used plumber's putty to attach geophones to bare outcrop surfaces (Figure 2a). To estimate bedrock velocity, we calculated distances from each shot point to all geophones and plotted them against the arrival times (Figure 2b). Because the traveltimes are a linear function of distance, the inverse slope of a least squares linear regression is an estimate of the velocity of the outcrop (Figure 2b). To check for lateral velocity variation, we performed a tomographic inversion following the Monte Carlo methods described in the supporting information using starting velocities between 3.3 and 3.8 km/s and gradients between 150 and 250 m/s/m (Figure 2c).

Light detecting and ranging (LIDAR) data acquired in September 2014 were used to extract elevations (Figure 1). The LIDAR topography was crucial to moving from the 2-D domain of the velocity surveys to the 3-D domain of our final products. Prior to interpolating the 2-D profiles into 3-D, we verified seismic velocities at transect intersection points by extracting velocity-depth functions and identifying

Table 1

Geometric Information of the 25 Seismic Refraction Profiles

Line number	Line name ^a	Date collected	Geophone spacing (m)	Shot spacing (m)	Seismic line length (m)	Final RMS (ms) ^b
1	BW_051713	5/17/13	4	16	190	1.84
4	BW_060713_1	6/7/13	2.5	15	240	1.80
5	BW_060713_2	6/7/13	2.5	15	240	2.22
6	BW_060713_3	6/7/13	2.5	15	240	1.90
7	BW_060713_4	6/7/13	2.5	15	240	2.31
8	BW_061713_1	6/17/13	2.5	15	240	1.85
9	BW_061713_2	6/17/13	2.5	15	240	1.57
11	BW_070313	7/3/13	2.5	5	240	1.78
12	BW_070813	7/8/13	2.5	10	240	2.29
13	BW_071013	7/10/13	2.5	10	240	1.75
14	BW_071213	7/12/13	2.0	8	192	1.59
15	BW_071513	7/15/13	2.0	8	192	1.76
16	BW_071713	7/17/13	2.0	8	192	1.53
17	BW_071913	7/19/13	2.5	10	240	1.61
18	BW_072613	7/26/13	2.5	15	240	1.79
19	BW_080414_2	8/4/14	2.5	10	300	1.88
20	BW_080514_1	8/5/14	2.5	10	300	2.00
21	BW_080514_2	8/5/14	2.5	10	300	1.69
22	BW_080614_1	8/6/14	2.5	10	300	1.64
23	BW_080614_2	8/6/14	2.5	10	300	1.69
24	BW_080714_1	8/7/14	2.5	10	300	1.85
25	BW_080714_2	8/7/14	2.5	10	300	1.77
26	BW_092715_1	9/27/15	1.0	5	191	1.62
27	BW_092715_2	9/27/15	1.0	5	191	2.26
28	BW_080115_2	8/1/15	2	8	190	1.83

^aThe line name corresponds to the name of the profile on the WyCEHG database (<http://wycehg.wygisc.org>). ^bThe final RMS is the RMS through the average of all 50 models from the Monte Carlo simulations (supporting information).

discrepancies; mismatched data sets were repicked and reinverted to achieve the best possible match. This helped improve consistency in velocity inversions across the surveys. Because our lines cross each other at several locations, we were able to test for the presence of seismic anisotropy (i.e., differences in velocity as a function of survey orientation). Although our analysis suggests that some anisotropy is present (details in the supporting information), we ignore it here because it is too small (less than 10%) to influence the main conclusions of this paper.

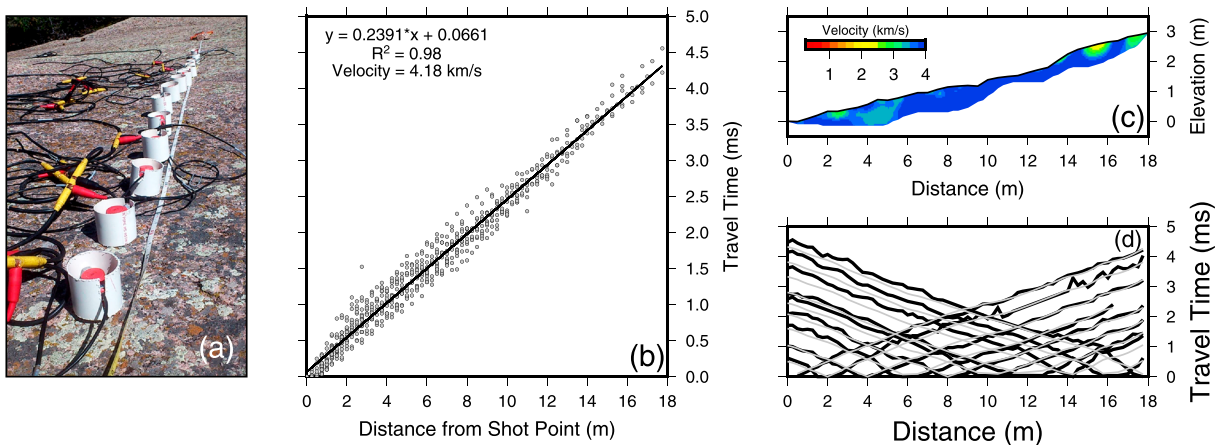


Figure 2. Seismic refraction results from an outcrop of Sherman granite. (a) Image of geophone setup on the outcrop; note the lack of fractures on the surface of the outcrop. (b) First-arrival traveltimes plotted as a function of distance from the shot point. The slope of the line is inversely related to the velocity, assuming no lateral or vertical subsurface heterogeneities. (c) Tomographic inversion following the Monte Carlo methods in the supporting information. When all pixels in model are averaged, the average velocity is 4.1 km/s. (d) Modeled and observed traveltimes. The final model had an RMS error of 0.15 ms.

Table 2
Water Depths and the Interpreted Weathered Bedrock Boundary^a

Well	Minimum water depth (m)	Maximum water depth (m)	Mean water depth (m) ^a	Depth of 1.2 km/s velocity (m)	Depth of 1.06 km/s velocity (m)	Depth of 1.34 km/s velocity (m)
BW-5	10.3	11.6	11.0	16.3	12.6	18.9
BW-2	10.5	11.8	11.1	15.3	11.6	16.5
BW-1	12.1	13.4	12.7	10.6	7.2	16.1
BW-4	9.6	11.5	10.5	13.3	9.6	15.6

^aWater level measurements from 4 February to 4 June 2016.

3.2. Drilling and Sampling

To relate seismic velocities to fracture density, state of weathering, and physical characteristics of the CZ, we drilled five boreholes in the study area (Figure 1). Our drilling permit required all boreholes to be within 30.5 m (100 feet) of maintained roads, limiting borehole locations to the ridge top. Borehole locations were selected to sample CZ structure and composition across a range of seismic velocity structures, including areas where velocities less than 2 km/s extend to deep (~40 m, BW-1 and BW-4), shallow (~10 m, BW-3), and intermediate depths (~30 m, BW-2 and BW-5). BW-1, BW-2, and BW-3 were drilled in November 2014 and reached depths of 31.7, 16.5, and 39.6 m, respectively. BW-4 and BW-5 were drilled in July 2015 and reached depths of 60.4 and 39.6 m, respectively. Each borehole was drilled with air and a rotary bit until a solid interface was encountered. After casing was set, core was recovered from deeper depths in more intact weathered rock using a rotary drill, producing 2.5" (6.35-cm) diameter core from BW-2, BW-3, BW-4, and BW-5 and 3.0" (7.62-cm) diameter core from BW-1. Cores were photographed using a Geotek core logger with a Sigma 105-mm microlens. Shortly after drilling, a Mount Sopris QL40-OBI-2G Optical Televiewer was deployed to provide a 360° unwrapped optical borehole image (OBI). Groundwater levels were logged continuously in four of the five wells from 4 February to 5 June 2016 using an in situ pressure transducer. The observed water levels were corrected to manual measurements made approximately once a month. The date range spanned by our observations, although limited, capture the spring runoff, which provides the largest observable change of groundwater levels. Four wells on the ridge (BW-3 excluded) show an average depth to water of 10.6 m (Table 2).

3.3. Moving From 2-D Profiles to a 3-D Seismic Velocity Volume

We used ordinary kriging to generate a 3-D volume of seismic velocities from our 25 two-dimensional profiles. Individual profiles are plotted as fence diagrams in two categories: ridge lines (Figure 3a) and valley lines (Figure 3b). The kriging volume consists of a 970 by 600 by 80-m rectangular prism with 10-m spacing in the horizontal dimensions and 1-m spacing in depth (Figures 3c and 3e). Unlike inverse distance or spline interpolations, kriging weights data based on spatial correlations (Bourges et al., 2012; Burrough et al., 2015; Dubrule, 1984; Remy et al., 2009; Wackernagel, 2003). Kriging identifies directional trends in the spatial statistics by calculating experimental variograms and fitting the trends with a model variogram (Nyquist et al., 1996).

To use kriging, we follow a four-step process (Figure 3d). First, we remove the landscape surface elevations by subtracting them from all profiles, which makes the 2-D subsurface data a function of depth. Using the depth data, we calculate experimental and model variograms using the Stanford Geostatistical Modeling Software (Remy et al., 2009) and Matlab (details in the supporting information). Once model variograms were found, we used ordinary kriging to estimate velocities at all locations in the 3-D volume. The ordinary kriging algorithm in Stanford Geostatistical Modeling Software (Remy et al., 2009) requires a search ellipsoid, which defines the maximum (here 50) and minimum (5) number of data points used for each interpolated value. The search ellipsoid has a diameter of 200 m in both the *x* and *y* directions and 4 m in the vertical direction. These parameters were selected by removing 50% of the 2-D data and generating 35 different volumes using different search ellipsoids with diameters ranging from 500 to 100 m in the *x* and *y* directions and 1 to 10 m in the *z* direction. Results showed that the search ellipsoid did not influence the final interpolation when the length of the ellipsoid in the vertical direction was a minimum of 4 m. After kriging is completed, we add landscape surface topography back to obtain a 3-D estimate of seismic velocities (Figure 3e). Interpolating in the 3-D domain is similar to interpolating in the 2-D domain (where depth is constant), but because the search

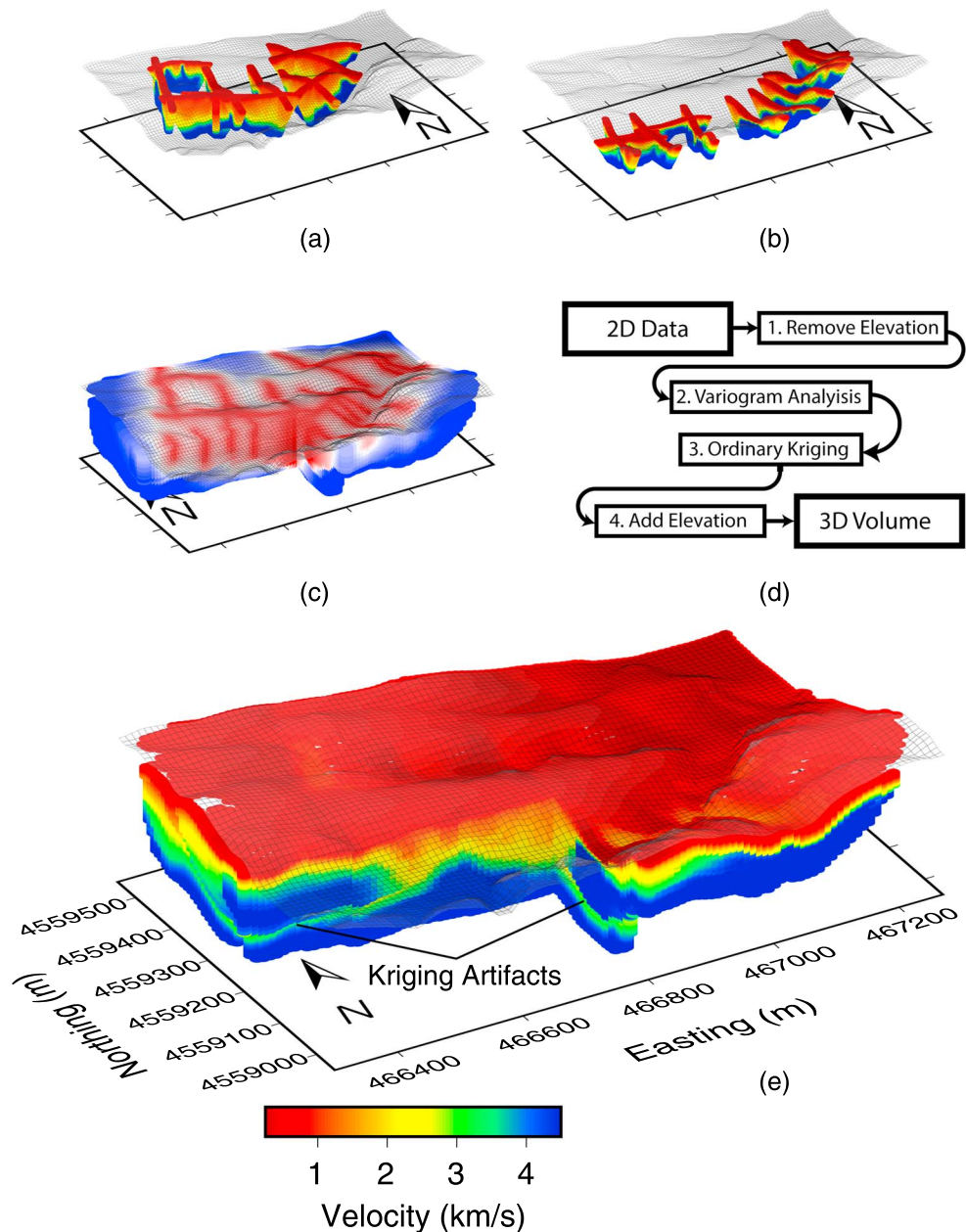


Figure 3. (a) Fence diagram of 2-D velocity profiles that cross or are on the ridge (lines 17–28 Table 1). (b) Fence diagram of 2-D velocity profiles located in the valley bottom (lines 1–16 Table 1). (c) The kriging variance volume, used to remove artifacts (green stripe in e). (d) Generalized flow chart for processing 2-D data (a and b) into a 3-D volume (c and e). (e) The 3-D volume of seismic velocities found through ordinary kriging using the experimental variograms defined in the supporting information. The extent of the kriging volume is shown by the blue bounding box in Figure 1.

ellipsoid has a nonzero length in the z direction, the 3-D interpolation provides continuity in velocity as a function of depth. No interpolation method will predict heterogeneity if it is not directly sampled, but the dense array of 2-D data should make the interpolated kriging volume a good estimate for velocity structure between profiles.

Kriging provides both a volume of seismic velocities (Figure 3e) and an estimate of their variance (Figure 3c). The kriging variance is a function of distance from measured data and the correlation calculated from the model variograms. Kriging is an exact interpolator, meaning that the variance is zero at known data points. The kriging variance shows where estimates are most reliable (Figure 3c), providing a basis for eliminating

interpolated values with unacceptably high uncertainty. In this case, we removed velocities that had a kriging variance greater than $2 \text{ km}^2/\text{s}^2$. This culling criterion excluded a low-velocity artifact in the southern part of the volume (Figure 3e).

4. Results

We present our data as they relate to three layers of the CZ: protolith, weathered bedrock, and saprolite. Our site is soil mantled, but soil thickness is smaller (maximum = 107 cm) than the vertical resolution of the geophysical methods, so it is grouped in our analysis with the saprolite. We discuss the subsurface layers from the bottom up, reflecting the evolution of protolith to saprolite on its journey upward through the profile as the landscape surface erodes away. Thus, we adopt a perspective of the CZ as a throughflow reactor in which mass loss due to erosion at the surface is replaced by conversion of protolith to weathered rock and from weathered rock to saprolite at depth. For our purposes, protolith is rock that is essentially unaltered from its original state, with only minor chemical weathering and fracturing. Weathered bedrock is more extensively fractured and shows chemical alteration, mostly along and around fractures. Saprolite is pervasively weathered and friable but still retains the original fabric of the rock. In the following sections we provide observations from both borehole and seismic refraction data and use them to describe physical and chemical characteristics of the protolith, weathered rock, and saprolite at the BW study site.

4.1. Protolith

Our short refraction survey over exposed and relatively unweathered Sherman granite outcrop yielded an average velocity of 4.2 km/s from linear regression ($R^2 = 0.98$; Figure 2b) and 4.1 km/s (with minor lateral variation) by averaging the 2-D tomographic inversion (Figure 2c). The tomographically modeled data had a final RMS misfit of 0.15 ms (Figure 2d). Based on these results, we infer that protolith has a velocity between 4.1 and 4.2 km/s. For simplicity in the discussion that follows, we assume that the 4 km/s velocity contour represents the interface between protolith below and weathered rock above. This should be reasonable given that depth differences among the 4.0, 4.1, and 4.2 km/s contours were minor in all seismic profiles. Because physical processes (e.g., frequency content and raypath coverage) and numerical processes (e.g., regularization and cell size) smooth the velocity models, the velocity contours represent the best approximation of the interpreted boundary but may not be exact. In the refraction data from our site, the top of the protolith is marked by a clear change in apparent velocity of first arrivals, where arrivals turn abruptly toward lower slopes on traveltimes curves (Figure 4d), indicating that this is the seismically significant boundary that likely corresponds with a change in chemical and/or physical properties. The 4 km/s contour lies at the base of a relatively steep vertical gradient in velocity (Figure 4c): on ridge lines (lines 17 through 28) it takes ~16 vertical meters to increase from 1 to 2 km/s (vertical gradient of ~62 m/s/m) but only 13 m to increase from 2 to 4 km/s (~150 m/s/m). The high gradient can be seen both in the velocity profile of line 17 (Figure 4a), which shows a thick region of velocities less than 2 km/s (Figure 4a), and in a sharp change in slope in the traveltimes curves between 25 and 75 m (Figure 4d). On valley lines (lines 1–16), velocities of 4 km/s occur within 5 to 10 m of the surface directly under the valley axis (Figure S1).

Drilling observations show that material with velocity of approximately 4 km/s is mostly unfractured and unweathered (Figure 5). One caveat is that only BW-4 extended deep enough to reach the 4 km/s boundary and BW-5 came within 3 m. Optical borehole images from those sections of borehole show that fractures within the material are limited to no more than one to three fractures per meter. Cores recovered from depths near the 4 km/s boundary show that oxidation-related staining is limited to fracture surfaces (Figures 5e and 5f). The material with velocity higher than 4 km/s is relatively unweathered but nevertheless probably has some preferential chemical weathering along the few fractures that are present. Together, these observations indicate that the material with $V_p > 4 \text{ km/s}$ is relatively intact protolith with less than one to three fractures per meter and minor chemical weathering along fractures.

Protolith topography (i.e., the surface defining the top of protolith) at our site is estimated by extracting the 4 km/s velocity contour from the 3-D volume of seismic velocities (Figure 6). Velocities with kriging variance greater than $2 \text{ km}^2/\text{s}^2$ were removed prior to contouring the protolith topography, so the final maps of depth to protolith contain gaps (Figures 6b and 6c). The most prominent feature in protolith topography is the depression below the ridge. The depression is not an artifact of the kriging interpolation and can be observed in individual seismic profiles, especially lines perpendicular to the ridge (lines 26, 19, and 20 in Figure S1 and

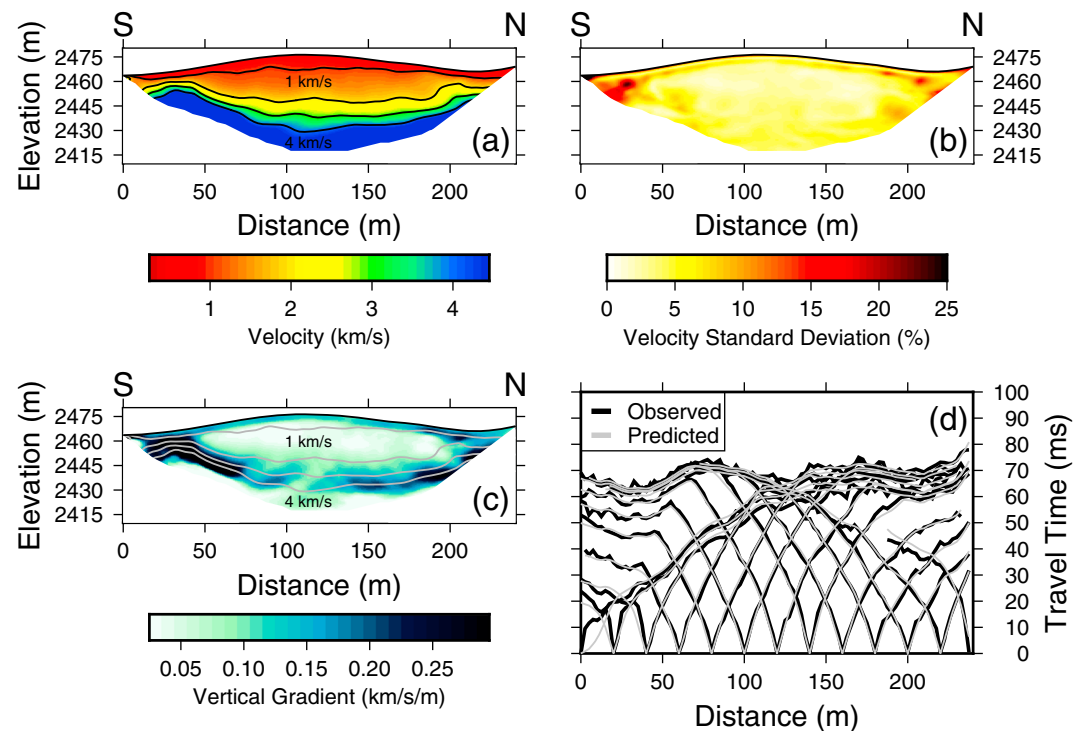


Figure 4. The seismic refraction inversion results for line 17. Masking was selected by removing all data below the deepest raypath and by using an aspect ratio mask, which removes most of the high-uncertainty data on the edges of the model. (a) The mean seismic velocity of the ensemble of 50 Monte Carlo simulations using 50 different starting velocity models. Velocity contours are shown in 1 km/s increments as solid black lines. (b) Standard deviation of velocities in the ensemble of 50 velocity models expressed as a percentage of the mean. (c) Vertical gradient of velocity with velocity contours shown in 1 km/s increments as solid gray lines. (d) Observed and predicted traveltimes for every other shot in the profile. Note the clear change in slope of first arrivals that occurs within 5 m of the valley shots but at ~50 m offsets on the ridge.

line 17 in Figure 4). Furthermore, the lines that cross valleys show 4 km/s at shallow depths (~10 m), whereas the lines running along the ridge show 4 km/s at much greater depths (~40–50 m, Figure S1). The protolith topography is inversely related to surface topography: it is concave up when the surface topography is convex up, with depths as high as 55 m beneath the ridge and as shallow as 2.8 m under valleys (Figures 6b and 6c). In map view, the bedrock depression follows surface contours, suggesting a strong surface-subsurface connection (Figure 6). The inverted protolith topography is similar to recent geophysical interpretations from Pond Branch, Maryland, and the Calhoun Critical Zone Observatory, in North Carolina (St. Clair et al., 2015), but this is the first time to our knowledge that the relationship has been observed in 3-D over a large area. Protolith topography also shows second-order heterogeneities spanning >10–20 m in scale. For example, in the southeast and northeast corners of the study area, we find humps in the protolith topography that produce unusually shallow thicknesses of overlying saprolite and fractured rock (Figure 6b). Both of these humps occur near or underneath areas of bedrock outcrop (Figure 1b). In addition, the ridge and underlying protolith topography is divided by a ~40-m wide north-south trending hump that divides the depression in the protolith topography into two basins (Figure 6) and is well constrained by the seismic profiles.

4.2. Weathered Bedrock

The weathered bedrock layer lies below the saprolite and above protolith and is characterized by slower refraction velocities (from 1.2 to 4 km/s), more intense fracturing, and obvious chemical weathering along fractures. Physical weathering is evident in the OBI data and core as numerous fractures (Figures 7a–7e). Visually, the material between the fractures (referred to here as the matrix) does not appear to be chemically weathered (Figures 7f–7j). However, chemical weathering is evident in this zone as stained fractures cutting through otherwise fresh-looking matrix minerals. Unlike the protolith boundary, the top of the weathered bedrock is not marked by a clearly defined velocity contrast. We can nevertheless pinpoint the top of

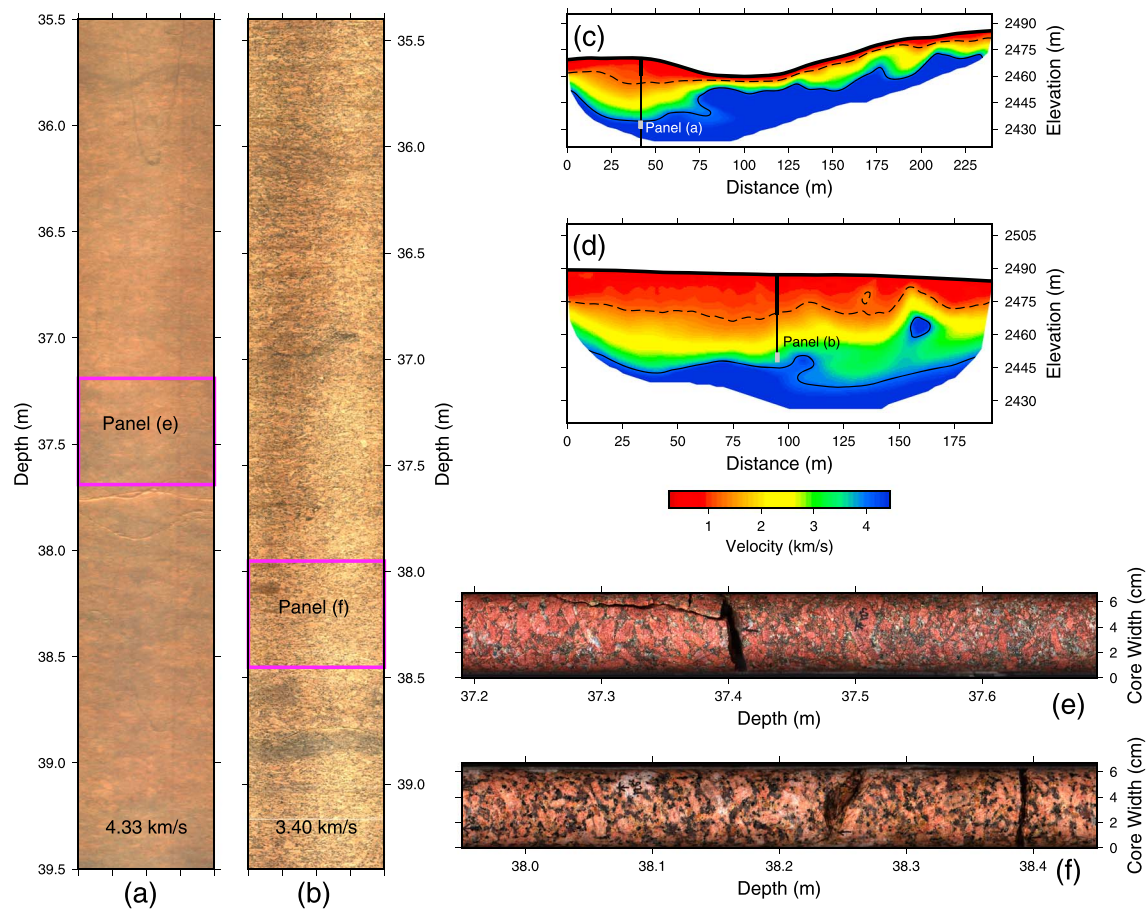


Figure 5. Physical state of the rock around the 4 km/s boundary. (a) Optical borehole image (OBI) over a 4-m interval of BW-4. Fractures are present but have fracture densities less than one to three fractures per meter. Surface seismic refraction velocity over this 4-m interval was 4.33 km/s. (b) Optical televiwer log over 4-m interval of BW-5. Again, a few fractures are present, but overall, the rock is mostly unfractured. The average refraction velocity over this depth interval was 3.4 km/s. (c) The 2-D velocity profile with the borehole location and casing depth (black bar) for BW-4. Gray bar shows vertical extent of OBI data in (a). (d) Velocity profile with the casing depth (black bar) and borehole location for BW-5. The gray bar shows the extent of the optical televiwer log in (b). (e) A subset of extracted core from the magenta box shown in a. (f) A subset of extracted core from the magenta box shown in b.

weathered bedrock throughout the ~ 45 million m^3 volume of investigation using two key observations: the depth of casing and visual inspection of material within this zone.

The depth of casing is set at the interface between mechanically weak material that may cause borehole collapse and competent material that is unlikely to cause borehole collapse. Drillers assessed material competence subjectively, by visual inspection of drill cuttings and by monitoring the pressure and drill bit advance rate. We suggest that the final depth is likely an overestimate of the depth to the base of saprolite under the assumption that drillers would generally want to ensure that casing is set in competent material. The fact that we could obtain core after casing was set is evidence that the casing base is near the transition from friable granite, interpreted as saprolite, to more intact rock that is fractured and weathered along fractures. The depth of casing varied by a factor of 3 across boreholes along the ridge, ranging from 6.1 to 18 m (Figure 8), whereas seismic velocities associated with this depth varied by less than 30%, from 1.06 to 1.35 km/s. The average velocity of material surrounding the casing bottom at the four holes on the ridge was 1.2 ± 0.14 km/s (mean \pm standard error; Figure 8). Thus, we interpret the top of weathered bedrock to correspond to the 1.2 km/s velocity contour. Increasing water saturation increases seismic velocity (Bachrach & Nur, 1998; Nur & Simmons, 1969), and without the drilling observations, it would not have been possible to differentiate this boundary from an increase in water content near the water table.

BW-3 is the only borehole that does not have a fracture density higher than 10 fractures per meter within the weathered bedrock (i.e., where $4.0 > V_p > 1.2$ km/s; Hayes, 2016). OBI data and recovered core from this

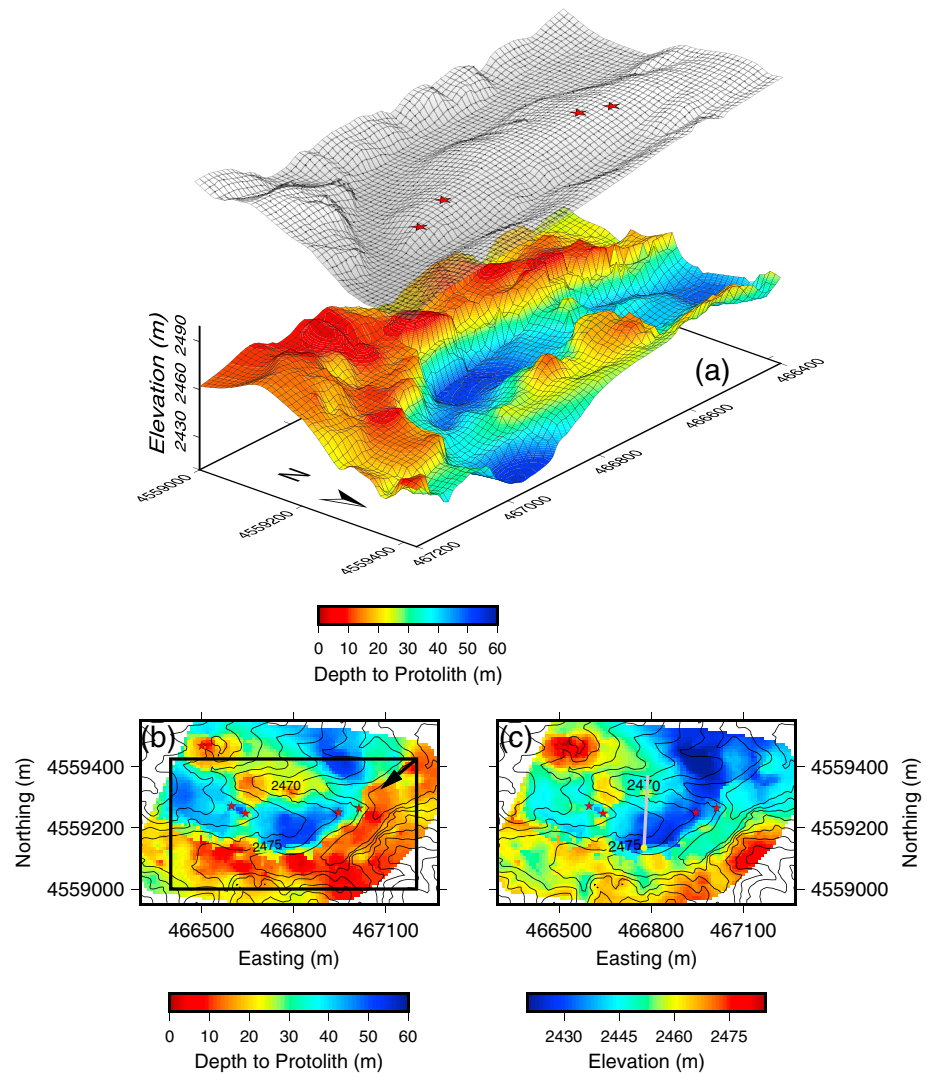


Figure 6. The 3-D images of the protolith surface generated by extracting the 4 km/s surface from the kriging volume. Red stars mark borehole locations in a–c. (a) The 3-D plot showing ground surface topography (gray) and protolith topography, where the latter is plotted using the protolith elevation (panel c) and then colored by depth to protolith (panel b). The depth of protolith was calculated by subtracting protolith elevation from surface elevation. The ground surface topography is shifted up 95 m for visualization purposes. Both surfaces have 2.5X vertical exaggeration. The orientation of this panel was selected to visualize the inverted protolith topography under the center ridge, and differs from the standard map view orientations shown in panels (b) and (c). (b) Depth below ground surface to protolith, with bounding black box showing area plotted in (a) and arrow identifying perspective in panel (a). (c) Map of absolute elevation (m asl) of protolith. Black lines represent 5-m contours of landscape surface topography in b and c. The gray profile is line 20, where the yellow circle indicates the start of the line.

borehole show minimal fracturing (Figure 7), consistent with the high velocity of 4.9 km/s encountered at just 7.5-m depth. More generally, however, visual inspection of the remaining boreholes reveals that the number of fractures decreases with increasing velocity, from 8 to 12 fractures per meter near the top of the casing to 1–3 fractures per meter near the top of protolith (Hayes, 2016). This decline in fracture density is correlated with the increase in seismic velocities with depth.

We extracted the surface defining the top of weathered bedrock from the 3-D seismic velocity volume by isolating the 1.2 km/s velocity contour (Figure 9). Although this surface is complex, it is roughly subparallel to the surface topography (i.e., convex up under the ridge). Thus, it differs from the protolith topography, which

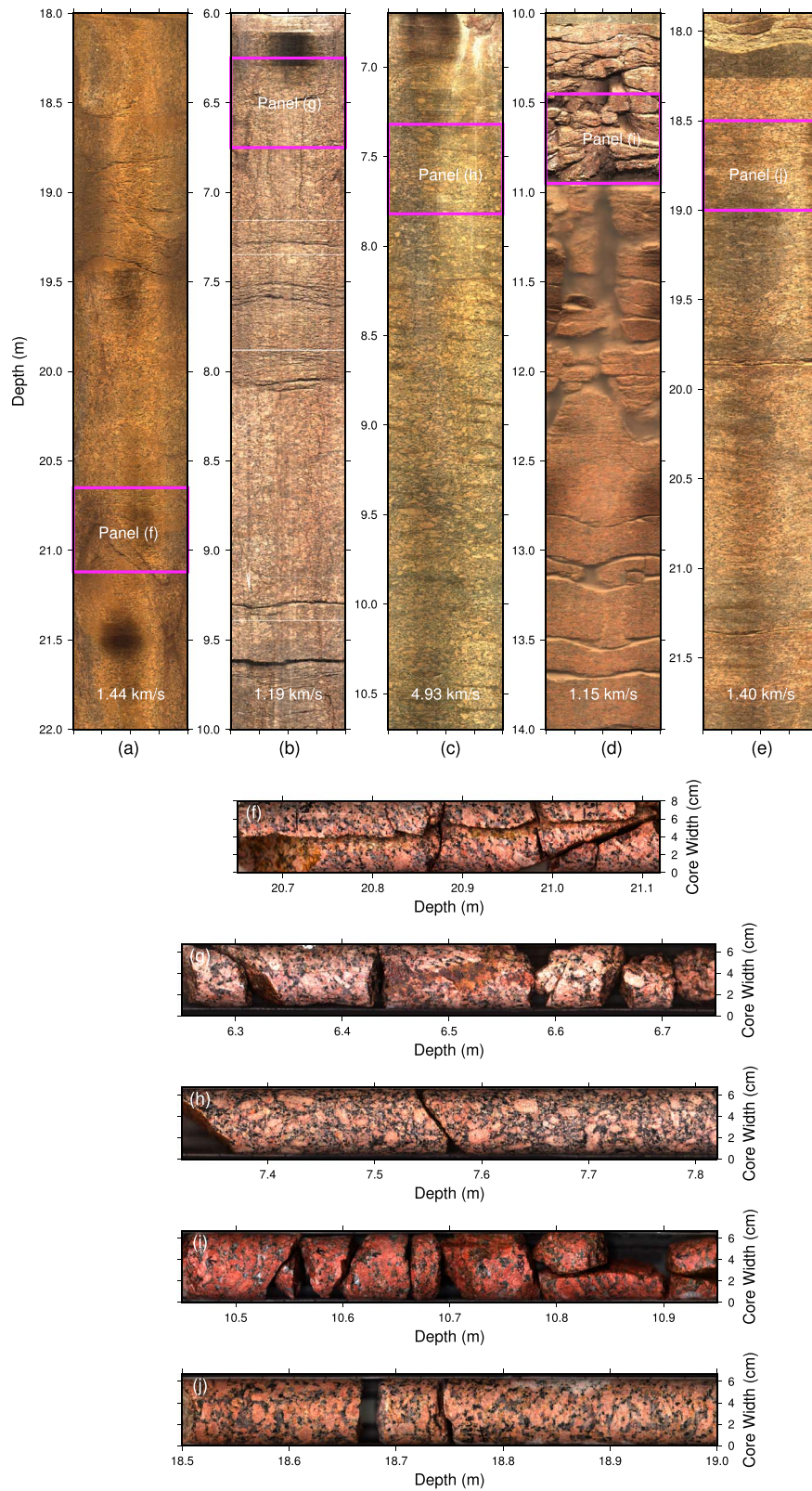


Figure 7. Images of rock immediately below casing at all five boreholes. (a–e) The first 4 m of optical televiewer data available from directly below casing. Labels in white text show the average velocity over the 4-m interval extracted from individual seismic refraction profiles. (a) BW-1, (b) BW-2, (c) BW-3, (d) BW-4, and (e) BW-5. (f–j) High-resolution photographs of 0.5-m intervals of the core. Magenta boxes in panels a–e show the approximate location of the core. The top of the core is on the left, and there is no lateral or vertical exaggeration in the images. (f) BW-1, (g) BW-2, (h) BW-3, (i) BW-4, and (j) BW-5.

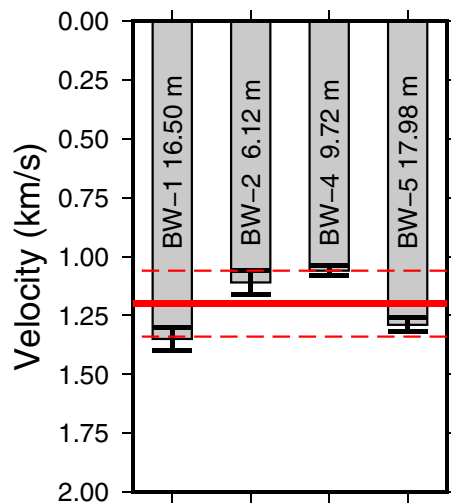


Figure 8. Velocity at casing depth for four boreholes on BW ridge. The depth of casing is labeled for each borehole and ranged from 6.12 to 17.98 m. The thick error bars represent the uncertainty in the tomographically derived velocity, in this case calculated as the standard deviation from the Monte Carlo analyses (supporting information). The bottom of casing, set by drillers at the uppermost levels where boreholes remained intact, varied over a narrow range in velocity (red lines: 1.20 ± 0.14 km/s) despite more pronounced variations in cased depth, which are labeled appropriately. BW-3 was excluded because it was not on the ridge.

roughly mirrors the topography of the landscape surface (i.e., concave up under the ridge). The weathered bedrock topography shows significant variability in the form of local depressions under the ridge (Figure 9b). These depressions are most notable under the western part of the ridge (Figure 9b), are greater than 10 m across, and are well constrained by the seismic velocity profiles (Figure S1). We calculated weathered bedrock thickness (Figure 9d) at each point on the landscape by subtracting the protolith surface elevations (Figure 6c) from the weathered bedrock surface elevations (Figure 9c). In general, the weathered bedrock is thickest under the ridge (~40–50 m) and thins out in adjacent valleys (<10 m; Figure 9d). Notable exceptions to these broad trends occur in the southeast and northeast corners of the study area where protolith crops out at the surface (Figure 1b).

4.3. Saprolite and Soil

The saprolite layer, which because of resolution limitations includes the relatively thin overlying layer of soil, extends from the ground surface to the top of weathered bedrock. We lack physical samples from the saprolite because the material was too friable to provide intact core during drilling, nor do we have OBI data in saprolite, because the boreholes were cased through this layer to prevent sidewall collapse. Samples collected via augering with a Geoprobe confirm that material is friable and porous to depths of at least 9 m at many locations within our study area. Controlled rainfall simulations measuring surface runoff on hillslopes near the BW study site suggest that rainfall rates as high as

180 mm/hr produce minimal overland flow (Carey & Paige, 2016). The lack of surface runoff is presumably due to high infiltration and storage capacity of thick, porous saprolite below the thin soil. To estimate the thickness of the saprolite and soil across the study area, we subtracted the elevation of the weathered bedrock surface (Figure 9c) from the surface topography. This produces a map of saprolite thickness, which is also equal to the depth to the top of weathered bedrock (Figure 9b). In our framework for interpreting the deep CZ, we assume that the saprolite layer has the highest porosity and is the most chemically weathered of our three conceptual layers.

5. Discussion

5.1. CZ Structure

Together, the borehole observations and the 45 million m^3 of inferred seismic velocities under the BW ridge provide an unprecedented view of physical characteristics of the deep CZ in a granitic mountain landscape. It allows us to identify two distinct surfaces, which we call the top of protolith and the top of weathered bedrock. In this framework, there are three distinct subsurface layers at the BW site: protolith, weathered bedrock, and saprolite.

The base of casing in the four boreholes on the ridge exhibited marked variations in depths and a relatively narrow range in observed velocity 1.2 ± 0.14 km/s (Figure 8). This velocity is lower than previously reported estimates of 2 km/s for the transition between saprolite and weathered bedrock in granitic terrain in the Sierra Nevada (Holbrook et al., 2014) and granitic gneiss elsewhere in the eastern Rocky Mountains (Befus et al., 2011). However, we argue that it is robust, based on our ability to recover core at deeper depths (but not at shallower depths) and OBI observations of fractured rock directly below casing (Figure 7). This saprolite-weathered rock interface is associated with a gradual rather than sharp change in seismic velocity. This is broadly consistent with observations from previous work that the boundary between saprolite and weathered rock is often gradational (Brimhall & Dietrich, 1987; Buss et al., 2013; Fletcher & Brantley, 2010; Graham et al., 2010). However, analysis of the velocity data alone is unable to determine whether this boundary is simply laterally heterogeneous (i.e., a thin weathering front with irregular depth) or a gradational zone (i.e., a thick weathering front or saprolite intermixed with corestones), or a combination of both.

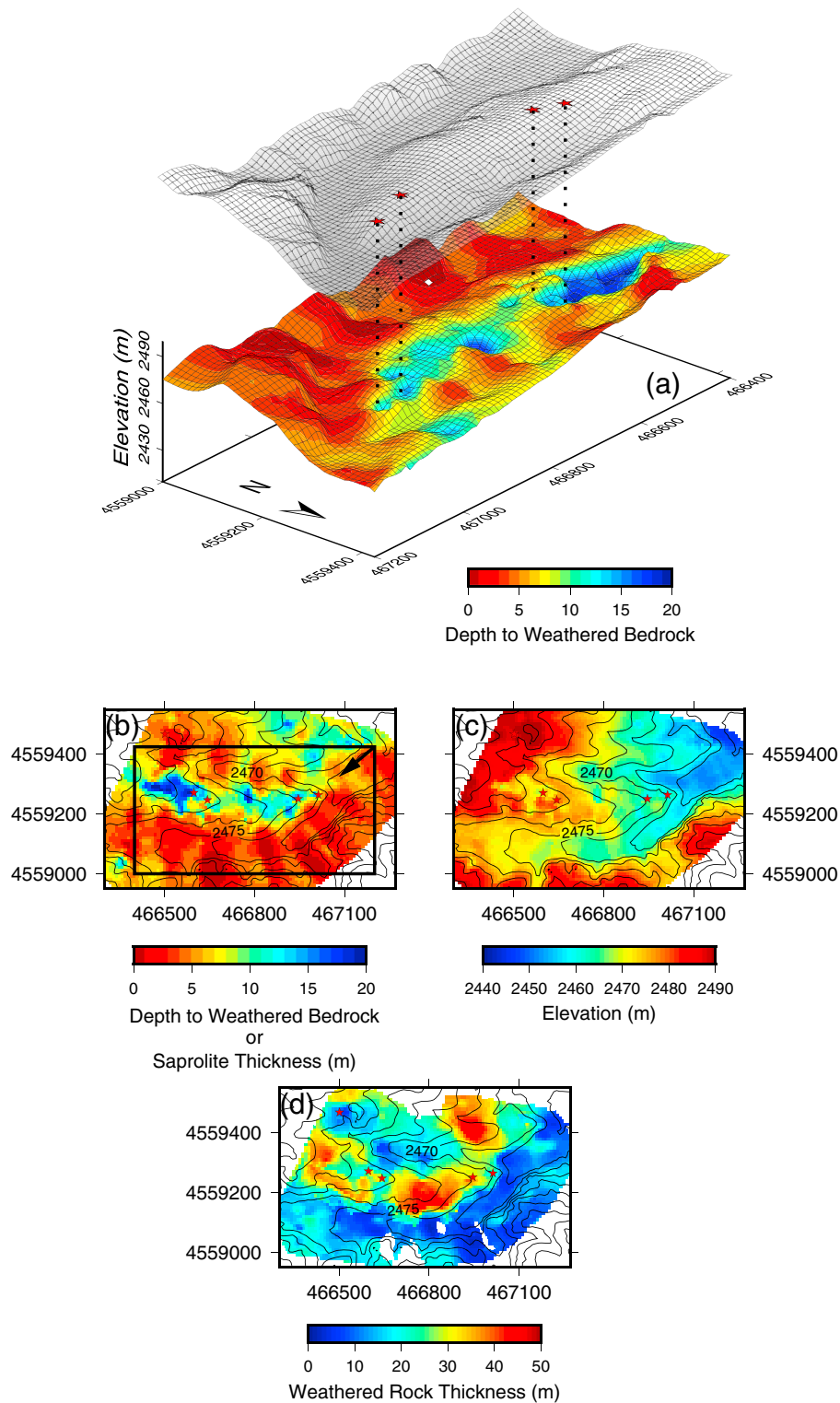


Figure 9. The 3-D images of the saprolite/weathered bedrock boundary created by extracting the 1.2 km/s velocity contour from the kriging volume. Red stars in each panel show boreholes. (a) Weathered bedrock surface colored by depth below the landscape surface plotted at 2.5X vertical exaggeration. The gray shaded surface shows the surface topography shifted up for visualization. Black dotted lines show the extent of casing in the four boreholes. The orientation of this panel was selected to be consistent with Figure 6a, and differs from the standard map view orientations shown in panels (b)–(d). (b) Map of the depth to weathered bedrock. Black box outlines area shown in (a), and arrow shows the perspective displayed in (a). (c) Map of weathered bedrock elevations. (d) Estimate of the weathered bedrock thickness, calculated by subtracting the weathered bedrock surface elevation (panel d) and the protolith elevation surface (Figure 6c). Black contour lines in b–d are 5-m contours of landscape surface elevation.

We found that protolith has a velocity of $\sim 4.1\text{--}4.2$ km/s (Figure 2), consistent with bedrock velocities found on granite outcrops in the Southern Sierra Critical Zone Observatory (Holbrook et al., 2014). OBI data from depths with these high velocities show solid rock with limited fractures (Figure 5). Furthermore, the velocity gradient in the vicinity of the 4 km/s contour is very steep (Figure 4c), indicative of a sharp contrast in material properties (Hayes, 2016). It is likely that fractures exist below the boundary we interpret as bedrock and may even initiate at depth as a result large-scale tectonic forces (Molnar et al., 2007). One possible hypothesis is that stresses at depths beneath the 4 km/s transition are sufficient to keep existing fractures closed. Such a stress threshold could provide an explanation to the observed sharp contrast in velocities. More work is needed to explore this hypothesis and evaluate the implications of this sharp velocity gradient for CZ processes.

The relationship between our proposed CZ boundaries and the locations of surface outcrops is not straightforward. The ridge is soil mantled and mostly devoid of outcrops (Figure 1d), but the hillslope to the south has abundant outcrops, and scattered outcrops occur in the northwestern corner of the study area (Figure 1b). To add another layer of complexity, all three types of Sherman granite (Sherman, Lincoln, and porphyritic) occur in outcrops in the study area, though the prevalence of both the Lincoln and porphyritic varieties is minor by comparison, based on their limited occurrence in the cores. Core recovered from BW-1, BW-2, BW-3, and BW-5 is Sherman, while only BW-4 has the material that we would classify as porphyritic Sherman (Figure 7).

In the next sections, we use our observations of CZ structure to explore mechanisms controlling the relationship between landscape surface and the weathering interfaces at depth. In particular, we consider the bedrock drainage model of Rempe and Dietrich (2014), the topographic stress model of St. Clair et al. (2015), and the frost cracking model of Anderson et al. (2013). In the absence of data on chemical weathering as a function of depth and the lack of a known relationship between chemical weathering indices and seismic velocity, we are unable to explore the possible role of vertical (Lebedeva & Brantley, 2013) and lateral (Braun et al., 2016) flow of chemically reactive waters in setting the thickness of the CZ. However, each of the models that we can explore focuses on a distinct process of weathering and landscape evolution using quantifiable topographic attributes and defines boundaries that should produce a measurable change in seismic velocities. Because the models predict distinct subsurface patterns in weathering, it should be possible to use our seismic and borehole data to evaluate their relative importance in controlling CZ structure across the study site (Riebe et al., 2017).

5.2. Topographic Stress Hypothesis

According to the topographic stress model, topography perturbs the ambient stress field induced by regional tectonics and gravity. The resulting ambient stress field influences the type and distribution of near-surface fractures, which together control the ability of reactive fluids from the surface to enter and weather the rock (Martel, 2006, 2011; Miller & Dunne, 1996; Molnar et al., 2007; Moon et al., 2017; Slim et al., 2014; St. Clair et al., 2015). To explore this hypothesis, St. Clair et al. (2015) conducted seismic refraction surveys at three sites with distinctly different predictions for the three-dimensional subsurface stress field, summarized by two scalar proxies: failure potential and least compressive stress. The combination of high failure potential and low least compressive stress contributes to higher probabilities of forming, reactivating, or opening fractures. In areas under high tectonic compression, the stress model predicts that the lower limit of abundant open fractures should mirror the surface topography (i.e., a concave upward surface), creating a characteristic bow tie shape of thick weathered material under the ridge and thin weathered material in the valleys. Conversely, in areas under low tectonic compression, the lower limit of abundant and open fractures should parallel the surface topography (i.e., a convex downward surface). Subsurface weathering observed in St. Clair et al.'s (2015) geophysical surveys matched predictions from the model at each of the three study sites. This model argues that topographic stress can exert strong control on the geometry of deep weathering surfaces. Although measurements of regional stress are lacking near our site, predictions from a geodynamic model of gravitational potential energy and mantle dynamics suggest that our site lies at the transition between neutral/tensional stress in the Colorado Rockies to a compressive regime to the northeast (Ghosh et al., 2013).

To evaluate the topographic stress model in greater detail, we calculated the subsurface stress field at our site using a 2-D boundary element model (Slim et al., 2014; Figure 10 and supporting information). At the BW site, despite the second-order heterogeneities, the large-scale protolith topography is broadly consistent with the bow tie shape predicted in highly compressional tectonic regimes. Based on this observation, we ran a series

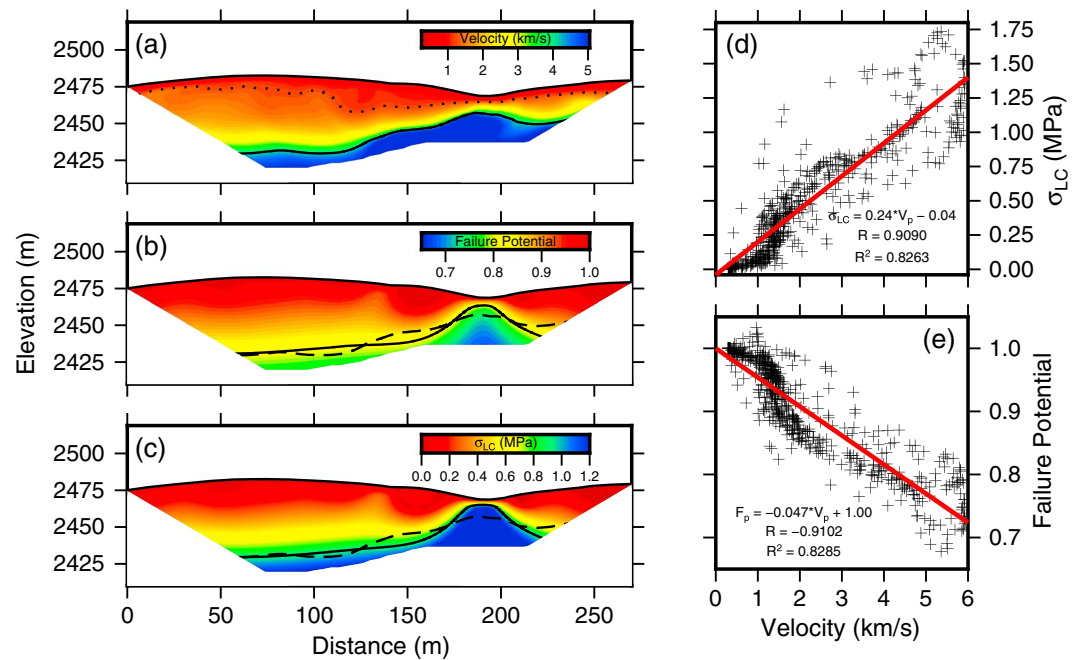


Figure 10. Results from a topographic and regional 2-D stress calculation along line 20 (Figure 1) assuming 8-MPa regional compression. All profiles are masked by the lowest raypath and the aspect math that was applied prior to kriging. (a) P wave velocity model derived from the shallow seismic refraction survey. The dotted line is the interpreted weathered bedrock boundary (1.2 km/s), and the solid line at depth is the interpreted protolith boundary (4.0 km/s). (b) Calculated failure potential, with lower values indicating where the rock is less likely to fail. The solid line marks a value of 0.81, which approximates the observed protolith boundary according to the linear relationship shown in panel (e). The dashed line is the 4 km/s velocity contour, which represents the seismically interpreted protolith boundary shown in panel (a). (c) The least compressive stress (MPa), where higher values indicate that fractures are likely to be closed. The solid line shows a value of 0.92 MPa, which approximates the observed protolith boundary according to the linear relationship shown in panel (d), and the dashed line is the interpreted protolith boundary from panel (a). (d) The relationship between the least compressive stress and seismic velocity is nonlinear, but the red line shows linear least squares regression to demonstrate a positive correlation ($R^2 = 0.83$). (e) The relationship between failure potential and seismic velocity is also nonlinear, but the red line shows linear least squares regression to demonstrate the negative correlation ($R^2 = 0.83$).

of models with horizontal compressive stress magnitudes ranging from 1 to 10 MPa. The model with a regional compression of 8 MPa had the strongest correlations between least compressive stress and velocity ($r^2 = 0.83$; Figure 10d) and between failure potential and velocity ($r^2 = 0.83$; Figure 10e). Using the linear regression fits (Figure 10), we calculated values of least compressive stress (0.92 MPa) and failure potential (0.81) corresponding to our observed protolith velocity (4 km/s). We hypothesize that when failure potential and least compressive stress are higher than these values, existing fractures begin to open and intact rock is more likely to fracture. Both failure potential and least compressive stress follow the inverted shape (i.e., deep under the ridge and shallow under the valleys) of the protolith topography along profile 20 (Figure 10) when we assume that the region is under regional compression. Thus, the model output is consistent with the generation of open fractures under gradients in topographic and regional stresses as an important control on protolith topography in the deep CZ at the BW site.

To more rigorously evaluate the role of topographic stress on bedrock topography in the region, we would need to measure the magnitude and direction of the regional stress field and calculate the resulting topographic stress field in 3-D for comparison with the observed protolith topography in our 45 million m^3 kriging volume (Figure 6), and not just assume compression as we did in this case. However, given the generally smooth landscape topography of the region (Figure 1), even a detailed 3-D subsurface stress model with linear elastic, homogeneous, and isotropic material would most likely not be able to explain the observed second-order structures of the protolith topography such as the occurrence of outcrops on the hillslope south of the ridge and in the northwestern part of the study area, nor could it explain the marked roughness of the protolith topography under the ridge (Figure 6).

5.3. Bedrock Drainage Hypothesis

Regional patterns of groundwater drainage under ridge and valley topography may dictate spatial patterns of subsurface weathering (e.g., Goodfellow, 2012; Manning & Caine, 2007; Toth, 1999). To explain the relationship between topography, drainage, and subsurface weathering in a steep landscape underlain by argillite, Rempe and Dietrich (2014) proposed a 1-D steady state model coupling erosion and groundwater flow. In this model, channel incision drives erosion that exhumes fresh bedrock toward the surface, which in turn creates an elevation gradient between hillslopes and channels and hydraulic gradients at depth. The hydraulic gradients drive drainage of chemically equilibrated water from bedrock on geologic timescales. As bedrock is drained, it becomes susceptible to chemical attack by reactive fluids from the surface, leading to downward advance of the weathering front. The model predicts that channel incision and bedrock hydraulic conductivity control the evolution of bedrock topography, because of their influence on the minimum elevation of the water table, which regulates the position of the weathering front. In essence, the model posits that weathering is limited to the maximal extent of the vadose zone. Hence, the model predicts a convex weathering front that broadly follows topography, producing a weathered layer that is thickest at the center of the ridge and thins toward the valley. If the landscape has a slow incision rate and if the bedrock has low hydraulic conductivity, the variation in weathering zone thickness from ridge to valley is especially pronounced.

However, our site differs from the system modeled by Rempe and Dietrich (2014) in that it is likely the interface between saprolite and weathered bedrock that coincides with the strong hydraulic conductivity contrast. This may often be the case in granitic terrain (Katsuyama et al., 2010; Ruxton & Berry, 1957, 1959). Thus, flow through weathered bedrock, with its low hydraulic conductivity, may behave much as it does in the fresh (unweathered) argillite of the system modeled by Rempe and Dietrich (2014). We therefore posit that the interface between saprolite and weathered bedrock is controlled by the local hydraulic gradients resulting from local channel incision, linking the interface between saprolite and weathered bedrock to the evolution of surface topography, consistent with the mechanism proposed by the Rempe and Dietrich (2014) for explaining the fresh-bedrock surface. If we assume a large hydraulic conductivity contrast between the saprolite and weathered bedrock and a slow local erosion rate, then the mechanism proposed by the bedrock drainage model could explain the topography of the saprolite-weathered bedrock interface. These assumptions seem reasonable given the low bedrock hydraulic conductivity typical of granite (Caine & Tomusiak, 2003; Long et al., 1982; Pratt et al., 1977) and the low erosion rates measured at sites nearby (Dethier et al., 2014; Dethier & Lazarus, 2006). At our site, the saprolite and weathered rock interface represents the maximal extent of the vadose zone. In relation to the specific language of Rempe and Dietrich (2014), our interpretation of the Blair-Wallis ridge is not consistent on the terms “weathered rock” and “unweathered rock,” but we nonetheless propose that the mechanism provides a plausible explanation for the topography of the saprolite-weathered bedrock interface (Figure 9).

We point to two observations in particular from the BW site that suggest that groundwater drainage may control the relationship between the ground surface and the interface between saprolite (grus with coarctones) and weathered bedrock (fractured bedrock, with an unweathered matrix and weathering along fractures). First, the observation that water levels occur slightly above or at the top of weathered bedrock (i.e., the 1.2 km/s contour in Figure 11 and Table 2) is consistent with the prediction that the weathering front is controlled by the lowest position of the water table (i.e., base of the vadose zone; Rempe & Dietrich, 2014). Our water table data for the site span less than 1 year but includes the spring snowmelt, which drives the largest annual fluctuation in groundwater height. Hence, it should provide at least a first approximation of the maximal extent of the vadose zone. The second observation is that the weathered bedrock boundary broadly resembles a subdued version of surface topography, with saprolite that is thicker under the ridge and thinner under valleys (Figure 9). Thus, we interpret the material above the saprolite-weathered bedrock boundary to be pervasively geochemically weathered and to have a much higher hydraulic conductivity than the material below, where weathering likely becomes concentrated along individual fractures.

Nevertheless, it is important to recognize that the bedrock drainage model (Rempe & Dietrich, 2014) fails to predict the boundary between weathered bedrock and protolith (Figure 6), which is the surface it was developed to simulate. Moreover, it does not predict any of the heterogeneities at the saprolite-weathered bedrock boundary (Figure 9). However, the broad agreement in the predicted and observed shape of the

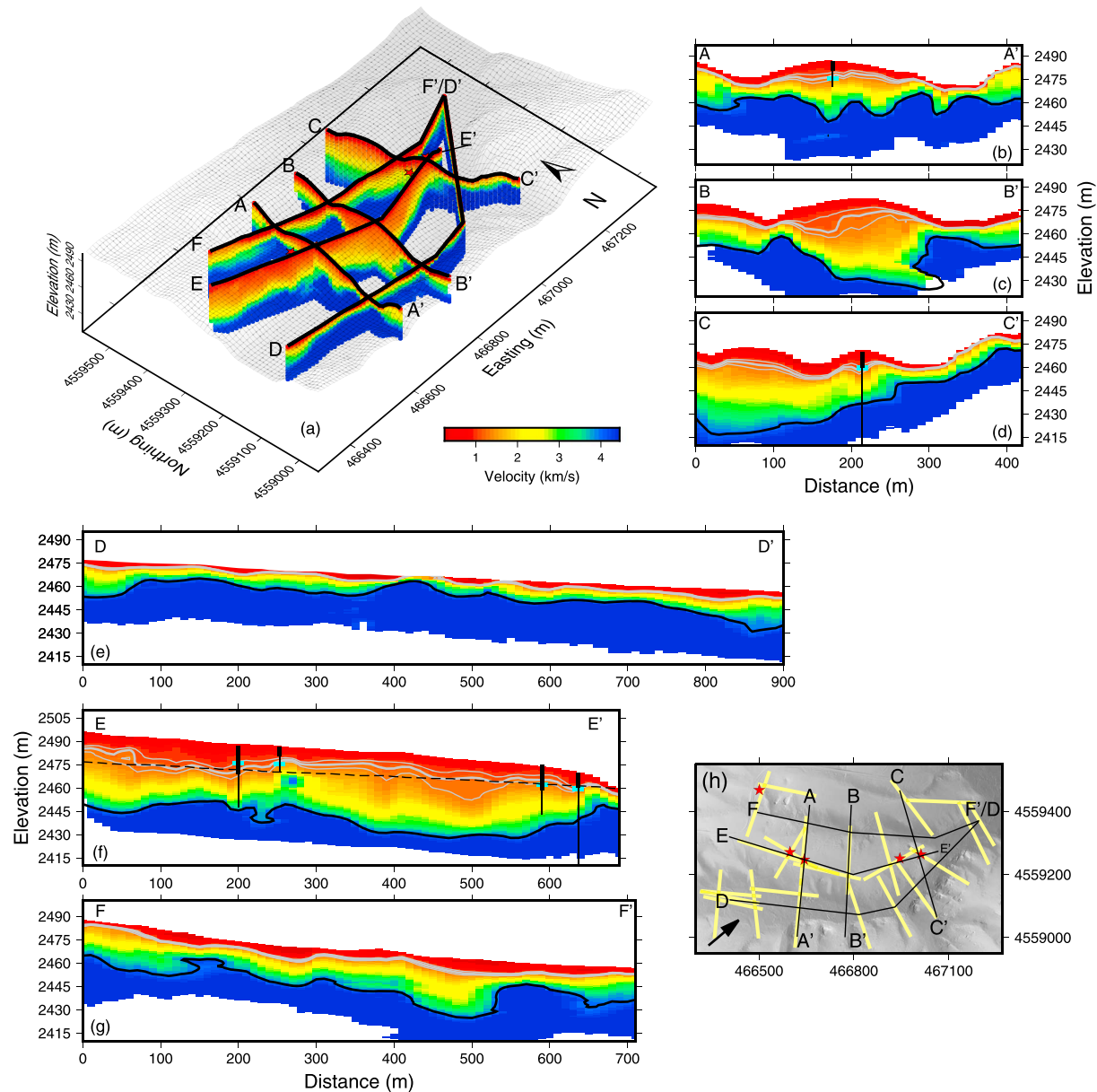


Figure 11. Extracted 2-D profiles from the velocity volume. All individual 2-D sections are plotted at 2X vertical exaggeration. We mark the interpreted weathered bedrock boundary (1.2 ± 0.14 km/s) with gray contour lines where the thicker line is 1.2 km/s and the thinner gray lines represent the uncertainty (i.e., 1.06 and 1.34 km/s, respectively). The interpreted protolith boundary (4 km/s) is marked by a thicker vertical line, and the total depth of the borehole is marked by a thin vertical line. Ranges of water depths in the boreholes are marked by two cyan lines, each representing the minimum and maximum observed water levels from 2/04/2016 to 6/4/2016 (Table 2). (a) The 3-D fence diagram ($2.5 \times VE$) showing the locations of individual extracted profiles. Red stars represent borehole locations. Orientation of the fence diagram is indicated by an arrow in panel h. (b) Transect A to A' ran perpendicular to the ridge and intersected BW-2. (c) Transect B to B' ran perpendicular to the ridge but did not intersect a borehole. (d) Transect C to C' was perpendicular to the ridge and intersected BW-4. (e) Transect D to D' ran down the southern valley, with no boreholes along the transect. (f) Transect E to E' ran parallel to the valley line in panel e and intersected all four ridge boreholes. Boreholes in the figure are BW-5, BW-2, BW-1, and BW-4 from west to east (left to right). The minimum elevation of the southern valley is overlain in panel f as a dotted black line, demonstrating that it is close in elevation to the interpreted weathered bedrock boundary (1.2 km/s). This also shows that the depth to water is just above or equal in elevation to the southern valley, indicative of a low hydraulic gradient from ridge top to stream valley. (g) Transect F to F' was extracted along the axis of the northern drainage and did not intersect boreholes. This profiles is the least constrained of all six extracted profiles. (h) Inset map showing the location of the extracted transects in relation to the topography. Transparent yellow lines show the seismic profile locations, solid black lines show the locations of the extracted transects (panels b–g), and the arrow in the lower left corner illustrates the perspective of the fence diagram in panel a.

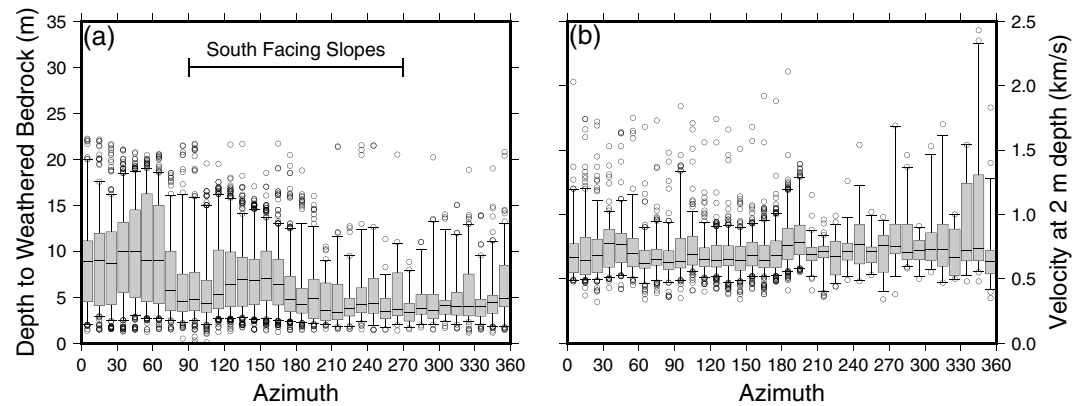


Figure 12. Regolith structure versus azimuth where 0°/360° is north, 90° is east, 180° is south, and 270° is west. (a) Depth to top of weathered bedrock ($V_p = 1.2$ km/s) and (b) seismic velocity at 2 m below the surface on all 25 seismic refraction profiles. Data in each bin are represented by a box and whisker plot where the center of the box is the median, the size of the box represents the 25 and 75% percentiles, and whiskers represent the 5% and 95% percentiles. Open circles are outlying data points.

surface supports the use of the bedrock drainage model to explain the relationship between topography and the weathering front at the base of saprolite.

5.4. Frost Cracking Hypothesis

The frost cracking hypothesis focuses on physical damage inflicted on rocks in the CZ by freezing water (Anderson et al., 2013). Frost cracking occurs when temperatures lie between -3 and -8 °C—referred to as the frost cracking window (Walder & Hallet, 1985). When water is available to move to the freezing front and temperature is within the frost cracking window, water freezes in pore spaces and initiates new fractures. Because temperature is dependent on solar radiation, north-facing hillslopes tend to be cooler than south-facing ones in the Northern Hemisphere. Theoretical modeling of frost cracking has shown that over geologic time slight temperature discrepancies between north and south facing slopes can lead to thicker regolith on north facing slopes (Anderson et al., 2013). Regolith asymmetry was inferred in the Boulder Creek Critical Zone Observatory from seismic velocities (Befus et al., 2011). The Boulder Creek Critical Zone Observatory shares a similar elevation and climate with the BW site, so frost cracking could be a process shaping patterns observed in our data. This is corroborated by evidence of frost cracking near Vedauwoo, WY, just 3 km south of the study site (Anderson, 1998). Thus, it is reasonable to assume that damage caused by frost cracking might be detectable in our data (i.e., deeper than 2–3 m), with frost cracking damage resulting in slower seismic velocities. If frost cracking has an aspect dependence at our site and if frost cracking is an important weathering process at our site, we should be able to see it in slower velocities on north facing slopes and faster velocities on south facing slopes.

We tested for the aspect asymmetry predicted by frost cracking by plotting both the depth to weathered bedrock and the seismic velocity at 2-m depth as a function of aspect in 10° aspect bins across all 25 seismic profiles (Figure 12). To remove ambiguity, we focus only on the 2-D profiles, but this analysis can be extended to the entire volume and any arbitrary depth. The depth to weathered bedrock does not show a clear north-south aspect difference (Figure 12a). Northeast facing lines appear to have the deepest depth to weathered bedrock, but northwest facing lines show shallow depths to weathered bedrock. Moreover, if frost cracking is important, we would expect slower velocities at shallower depths on north facing slopes and faster velocities on south facing slopes, but no such difference is observed (Figure 12b). Hence, we suggest that our data do not support a difference in regolith structure related to north-south slope aspect.

The absence of aspect correlation may be due to the small topographic relief of our ridge, which could limit temperature differences on opposing slopes and thus produce frost damage that mimics the topography rather than differing with aspect. Even though we do not observe evidence of frost cracking in seismic velocity asymmetry, it likely plays an important role in causing subsurface rock damage at our site; our site falls within the correct temperature range, and water is commonly available, implying that frost cracking

almost certainly occurs, especially in topographic depressions where snowdrifts could accumulate. This may help explain some of the heterogeneity in the weathered bedrock surface. More work is needed to test this hypothesis.

5.5. Chemical Weathering Hypothesis

Given the gentle topography, thick subsurface zone of high porosity, and slow surface erosion rates of the site, it is likely that chemical weathering plays an important role in shaping subsurface CZ structure. As meteoric water infiltrates down through the subsurface, it reacts with surrounding minerals such as biotite (Buss et al., 2008; Fletcher et al., 2006; Goodfellow et al., 2016) or feldspars (Brantley & White, 2009; Maher, 2010). The reactions leave behind voids and weathering-induced fractures (Navarre-Sitchler et al., 2015) that reduce seismic velocities as they propagate through the medium. The porosity-generating weathering reactions can be modeled using reactive-transport equations that incorporate differences in surface erosion rates, mineral solubility, fluid chemistry, and reaction kinetics (Lebedeva et al., 2010; Maher & Chamberlain, 2014). These differences lead to separation of different mineral weathering fronts (Brantley et al., 2013), reflecting strong control of subsurface CZ structure that can be quantified using bulk geochemical measurements of subsurface samples (Brantley, Lebedeva, et al., 2017; Lebedeva & Brantley, 2013).

We have obtained extensive borehole logs, cores, and drill cuttings from the BW site. Visual inspection revealed an unweathered matrix with iron staining along individual fractures (Figure 7), but we have not conducted geochemical analyses on the material, nor did we model the propagation of weathering in the BW subsurface using a reactive transport models. Both tasks were beyond the scope of our primarily geophysical investigations. Without them, we cannot determine whether our interpreted physical boundaries match weathering boundaries predicted by geochemical models. Nevertheless, we recognize that chemical weathering and seismic velocity could be linked because of connections between porosity and seismic velocity (Berryman et al., 2002; Dvorkin et al., 1999; Nur et al., 1998), and moreover, we suspect that the connections are important to explaining variations in subsurface CZ structure at our site. In general, the relationships between weathering indices and seismic velocity are not well understood and represent an area of active research.

5.6. Complexity in CZ Structure

The models considered above ignore complications due to factors such as variations in bedrock geochemistry and hydraulic conductivity, which can be substantial on even the small scale of the BW ridge. Thus, they predict relatively simple and idealized CZ structure based mostly on topographic inputs. However, our geophysical observations clearly show that CZ structure is complex and heterogeneous on multiple scales across our site. This is true even though the velocity contours from the seismic tomograms represent unavoidably smoothed and inexactly located boundaries due to uncertainties driven by subsurface velocity gradients and seismic source frequency. Given this variability, we suggest that no single process-based model that has been developed thus far can explain the observed complexities in the CZ structure at our site, including the locations of outcrop on the surface. In general, the bedrock drainage model explains the location of the weathered bedrock boundary, under the seemingly reasonable assumption that the erosion rate is slow and the bedrock hydraulic conductivity is low. Meanwhile, the topographic stress model seems to provide a plausible mechanism to explain the inverted protolith topography, under the assumption that our site is in regional compression (which seems reasonable given available crustal stress models). Together, these models explain large-scale trends, but neither model alone or together is able to explain the second-order structure on interpreted weathering boundaries we observe.

One poorly constrained but nevertheless potentially confounding factor in this study is the effect of lithologic variations on weathering. Variations in bulk geochemistry can have a profound effect on rock weathering (Bazilevskaya et al., 2013; Brantley et al., 2013; Brantley & White, 2009; Hahm et al., 2014; Hilley et al., 2010; Lebedeva et al., 2007), so it is worth considering whether some of the observed heterogeneity in CZ structure can be explained by bedrock geochemical variability across our study area. Although bedrock geochemistry data are limited within the confines of our study area, the surrounding Sherman Batholith has been well studied, so bulk geochemical data are available for a wide range of sites spanning the region (Bell, 1998; Edwards & Frost, 2000; Frost et al., 1999; Galipeau & Ragland, 1979; Geist et al., 1989; Houston & Marlatt, 1997; Zielinski et al., 1982).

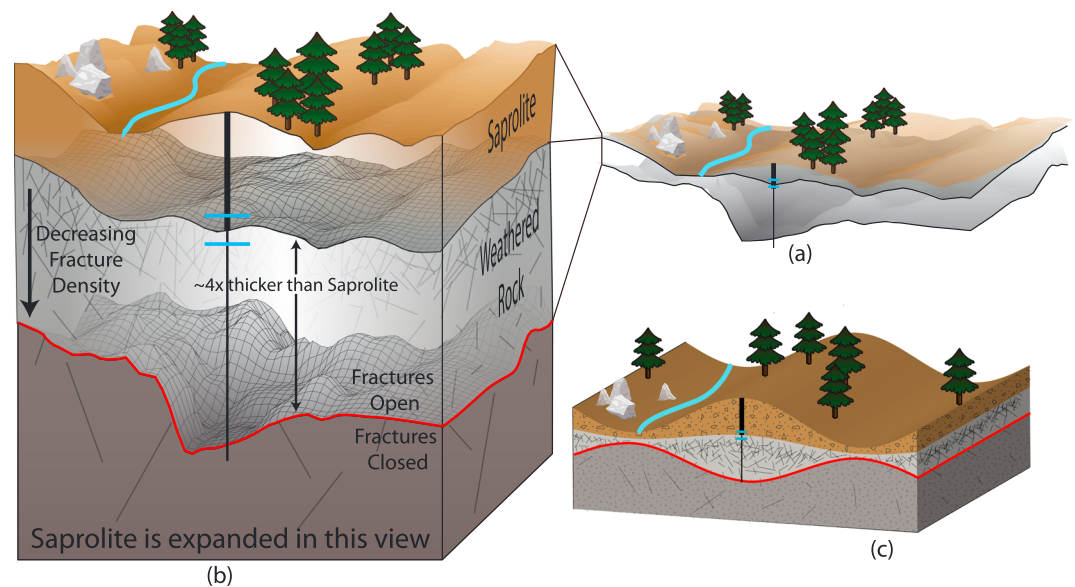


Figure 13. Conceptual model of CZ structure at the Blair Wallis site inferred from seismic refraction surveys and boreholes. We focus on two main boundaries: the division between weathered bedrock and saprolite and the division between weathered bedrock and protolith. In general, the upper surface of the weathered bedrock is convex upward, with thickest sections under the ridge and thinnest sections under valleys, corresponding to casing depths (thick vertical black line) and local water table measurements (cyan lines). The weathered bedrock is the thickest layer (~4 times the thickness of saprolite), and protolith topography is inverted relative to the surface topography on the center ridge. Vertical exaggeration highlights variability in the elevations of both the weathered bedrock and protolith surfaces. (a) Illustration showing the weathered bedrock and protolith boundaries with no vertical exaggeration. (b) The illustration is vertically exaggerated to show important processes and heterogeneity on both surfaces. (c) A simplified cross section showing the relationship between the saprolite, weathered bedrock, and protolith.

There is some indication that variations in bedrock geochemistry are playing a role in both surface and subsurface topography at the BW site. For example, a pronounced north-south ridge in protolith topography occurs underneath the large outcrop on the south side of the ridge (Figure 6). This appears to separate two basins with subsurface topography that seems inversely related to the surface topography (Figure 6). Although none of our profiles pass over visible outcrops, they are common on the hillslope directly across the southern valley and exist in a few locations on the ridge (Figure 1c). The north-south ridge in protolith occurs just east of a large outcrop on the ridge (Figure 1c). There is no change in surface topography above this rise in protolith topography, so it is unlikely that the topographic stress model will predict the north-south rise in protolith topography. Is this feature a result of changes in rock geochemistry? Is it an unmapped dike of Lincoln within the Sherman? Field observations suggest that Sherman and Lincoln weather differently. The Sherman tends to weather to round blocks, whereas Lincoln outcrops tend to weather to angular blocks. The Lincoln is more depleted of iron, magnesium, and calcium (Frost et al., 1999) potentially making it more weathering resistant than the Sherman. Changes in bulk geochemistry or the presence of dikes in the subsurface are two possible explanations for the heterogeneities we observe in the weathered bedrock and protolith boundaries. Additional data on the geochemistry of borehole core samples would help test this hypothesis.

Using 25 individually inverted 2-D seismic refraction transects, a host of borehole information from five cores, and a comprehensive geostatistical interpolation algorithm, we constructed a 3-D subsurface model of CZ structure across a ridge valley sequence (Figure 13). Although we are unable to identify a single model or process to explain observed CZ structure at our site, many of the coarse-scale features can be explained by combining the bedrock drainage model (Rempe & Dietrich, 2014) and the topographic stress model (St. Clair et al., 2015) for the evolution of the weathered rock and unweathered rock interfaces at depth. The 1.2 km/s surface fits the description of the weathering front described by the bedrock drainage model (Rempe & Dietrich, 2014); in general, it is convex upward, with a thicker weathered rock layer under ridges and thinner weathered rock layer under valleys. In addition, the water table depth at our site appears to be near this boundary

(Figure 13). However, close examination of this surface reveals second-order structures that the model cannot explain (Figure 13). The top of protolith, inferred here to be the 4.0 km/s surface, is similar in shape to surfaces of least compressive stress and failure potential based on a stress model assuming regional compression. The consistency between the stress model when we assume that the BW site is in regional compression (at around 8 MPa) and the 4 km/s boundary, or protolith surface, suggests that this boundary may represent an interface where fractures begin to open during rock exhumation through the ambient stress field. We propose that below the 4.0 km/s surface, the stress field keeps fractures closed, so protolith stays chemically unaltered. This controls the broad-scale structure of the deep CZ but cannot explain the roughness of the surface (Figure 13). More work is needed to test this hypothesis. Possible alternative explanations include geochemical variations, dikes of more weathering-resistant bedrock, and localized areas of frost cracking.

6. Conclusions

We combined geophysical data, which provide information over hundreds of meters vertically and laterally, with borehole data, which provide a plethora of information vertically at a single point on the landscape, to generate a 3-D image of subsurface weathering spanning ~ 45 million m^3 . We used these data to delineate boundaries dividing three CZ layers: saprolite, weathered bedrock, and protolith on the scale of hundreds of meters. In our landscape scale, 3-D image of CZ structure, saprolite has velocities less than 1.2 km/s, and weathered bedrock has velocities of 1.2–4 km/s, with visible chemical alteration along fracture planes, while protolith has velocities higher than 4.0 km/s and has little fracturing and chemical weathering. Our images reveal a complex CZ structure wherein the interfaces between readily distinguished layers have differing subsurface topography, suggesting that different physical, chemical, and biological processes act in different layers of the deep CZ.

We interpret the shape of the saprolite/weathered bedrock boundary to broadly reflect the drainage of chemically equilibrated fluid in fractured bedrock, similar to the process modeled by Rempe and Dietrich (2014). At deeper levels in the CZ, the top of protolith appears to correspond to the level below which the ambient stress field keeps fractures closed, significantly slowing groundwater flow below this boundary, as described by St. Clair et al. (2015). Although we lack supporting geochemical data, stained fractures are observed in cores extracted throughout the fractured zone, suggesting that chemical weathering processes (e.g., Brantley & White, 2009) affect the development of porosity in both saprolite and weathered bedrock, providing one possible explanation for the heterogeneity of the CZ structure. Although we did not observe aspect asymmetry, the site is in the correct temperature range for frost cracking to occur. Therefore, we cannot dismiss frost cracking as an important CZ process. Furthermore, none of the models presented predicts the surface outcropping of bedrock observed at the study site. Nonetheless, our results demonstrate that existing process-based models of deep weathering and fracturing need not be viewed as competing but rather can be treated as complementary in their influence on shaping distinct zones of weathering in the deep CZ.

Acknowledgments

This work was supported by NSFEP5-1208909, U.S. Army Research Office W911NF-14-1-0037, and NSF EAR-1331940. All data used in the publication are hosted on the Wyoming Center for Hydrology and Environmental Geophysics data discovery portal at <http://wycehg.wyisc.org> (doi: 10.15786/M2M37R). We thank the numerous undergraduates who helped with geophysical acquisition over two summers under the leadership of Mathew Provart. We also thank Austin Carey for discussion on the soils in the area, Daniel Beverly for discussion of vegetation within the study area, Bryan Shuman for the use of his core logger, and other University of Wyoming graduate students for their thoughtful discussions and constructive criticism of the manuscript. We are extremely appreciative of the four reviewers and Editor who took time to thoroughly read, inspect, and review this manuscript.

References

- Acworth, R. I. (1987). The development of crystalline basement aquifers in a tropical environment. *Quarterly Journal of Engineering Geology and Hydrogeology*, 20(4), 265–272. <https://doi.org/10.1144/GSL.QJEG.1987.020.04.02>
- Allen, P. A. (2008). From landscapes into geological history. *Nature*, 451(7176), 274–276. <https://doi.org/10.1038/nature06586>
- Andermann, C., Longuevergne, L., Bonnet, S., Crave, A., Davy, P., & Gloaguen, R. (2012). Impact of transient groundwater storage on the discharge of Himalayan rivers. *Nature Geoscience*, 5(2), 127–132. <https://doi.org/10.1038/ngeo1356>
- Anderson, R. S. (1998). Near-surface thermal profiles in alpine bedrock: Implications for the frost weathering of rock. *Arctic and Alpine Research*, 30(4), 362. <https://doi.org/10.2307/1552008>
- Anderson, R. S., Anderson, S. P., & Tucker, G. E. (2013). Rock damage and regolith transport by frost: An example of climate modulation of the geomorphology of the critical zone. *Earth Surface Processes and Landforms*, 38(3), 299–316. <https://doi.org/10.1002/esp.3330>
- Anderson, S. P., Anderson, R. S., & Tucker, G. E. (2012). Landscape scale linkages in critical zone evolution. *Comptes Rendus Geoscience*, 344(11–12), 586–596. <https://doi.org/10.1016/j.crte.2012.10.008>
- Anderson, S. P., Dietrich, W. E., & Brimhall, G. H. (2002). Weathering profiles, mass-balance analysis, and rates of solute loss: Linkages between weathering and erosion in a small, steep catchment. *Geological Society of America Bulletin*, 114(9), 1143–1158. [https://doi.org/10.1130/0016-7606\(2002\)114%3C1143:WPMBAA%3E2.0.CO;2](https://doi.org/10.1130/0016-7606(2002)114%3C1143:WPMBAA%3E2.0.CO;2)
- Anderson, S. P., von Blanckenburg, F., & White, A. F. (2007). Physical and chemical controls on the critical zone. *Elements*, 3(5), 315–319. <https://doi.org/10.2113/gselements.3.5.315>
- Bachrach, R., & Nur, A. (1998). High-resolution shallow-seismic experiments in sand. Part I: Water table, fluid flow, and saturation. *Geophysics*, 63(4), 1225–1233. <https://doi.org/10.1190/1.1444423>

- Bales, R. C., Hopmans, J. W., O'Geen, A. T., Meadows, M., Hartsough, P. C., Kirchner, P., et al. (2011). Soil moisture response to snowmelt and rainfall in a Sierra Nevada mixed-conifer forest. *Vadose Zone Journal*, 10(3), 786–799. <https://doi.org/10.2136/vzj2011.0001>
- Bazilevskaya, E., Lebedeva, M., Pavich, M., Rother, G., Parkinson, D. Y., Cole, D., & Brantley, S. L. (2013). Where fast weathering creates thin regolith and slow weathering creates thick regolith. *Earth Surface Processes and Landforms*, 38(8), 847–858. <https://doi.org/10.1002/esp.3369>
- Befus, K. M., Sheehan, A. F., Leopold, M., Anderson, S. P., & Anderson, R. S. (2011). Seismic constraints on critical zone architecture, Boulder Creek watershed, Front Range, Colorado. *Vadose Zone Journal*, 10(4), 1342–1342. <https://doi.org/10.2136/vzj2010.0108er>
- Bell, J. M. (1998). A petrographic, geochemical and isotopic investigation of the Mule Creek-Richeau Hills portion of the Sherman Batholith, Laramie, Wyoming (M.S.). University of Wyoming, United States-Wyoming. Retrieved from <http://search.proquest.com.libproxy.uwyo.edu/pqdtdlocal1005743/docview/304458004/citation/6AB9176C22074928PQ/1>
- Berryman, J. G., Pride, S. R., & Wang, H. F. (2002). A differential scheme for elastic properties of rocks with dry or saturated cracks. *Geophysical Journal International*, 151(2), 597–611. <https://doi.org/10.1046/j.1365-246X.2002.01801.x>
- Bourges, M., Mari, J.-L., & Jeannée, N. (2012). A practical review of geostatistical processing applied to geophysical data: Methods and applications—Geostatistical processing applied to geophysical data. *Geophysical Prospecting*, 60(3), 400–412. <https://doi.org/10.1111/j.1365-2478.2011.00992.x>
- Bradley, W. C. (1987). Erosion surfaces of the Colorado Front Range: A review. In W. L. Graf (Ed.), *Geomorphic systems of North America* (pp. 215–220). Boulder, CO: Geologic Society of America.
- Brantley, S. L., Buss, H., Lebedeva, M., Fletcher, R. C., & Ma, L. (2011). Investigating the complex interface where bedrock transforms to regolith. *Applied Geochemistry*, 26, S12–S15. <https://doi.org/10.1016/j.apgeochem.2011.03.017>
- Brantley, S. L., Eissenstat, D. M., Marshall, J. A., Godsey, S. E., Balogh-Brunstad, Z., Karwan, D. L., et al. (2017). Reviews and syntheses: On the roles trees play in building and plumbing the critical zone. *Biogeosciences*, 14(22), 5115–5142. <https://doi.org/10.5194/bg-14-5115-2017>
- Brantley, S. L., Holleran, M. E., Jin, L., & Bazilevskaya, E. (2013). Probing deep weathering in the Shale Hills Critical Zone Observatory, Pennsylvania (USA): The hypothesis of nested chemical reaction fronts in the subsurface. *Earth Surface Processes and Landforms*, 38(11), 1280–1298. <https://doi.org/10.1002/esp.3415>
- Brantley, S. L., Lebedeva, M. I., Balashov, V. N., Singha, K., Sullivan, P. L., & Stinchcomb, G. (2017). Toward a conceptual model relating chemical reaction fronts to water flow paths in hills. *Geomorphology*, 277, 100–117. <https://doi.org/10.1016/j.geomorph.2016.09.027>
- Brantley, S. L., & White, A. F. (2009). Approaches to modeling weathered regolith. *Reviews in Mineralogy and Geochemistry*, 70(1), 435–484. <https://doi.org/10.2138/rmg.2009.70.10>
- Braun, J., Mercier, J., Guillocheau, F., & Robin, C. (2016). A simple model for regolith formation by chemical weathering. *Journal of Geophysical Research: Earth Surface*, 121, 2140–2171. <https://doi.org/10.1002/2016JF00391>
- Brimhall, G. H., & Dietrich, W. E. (1987). Constitutive mass balance relations between chemical composition, volume, density, porosity, and strain in metasomatic hydrochemical systems: Results on weathering and pedogenesis. *Geochimica et Cosmochimica Acta*, 51(3), 567–587. [https://doi.org/10.1016/0016-7037\(87\)90070-6](https://doi.org/10.1016/0016-7037(87)90070-6)
- Brooks, J. R., Barnard, H. R., Coulombe, R., & McDonnell, J. J. (2010). Ecohydrologic separation of water between trees and streams in a Mediterranean climate. *Nature Geoscience*, 3(2), 100–104. <https://doi.org/10.1038/NNGE0722>
- Burrough, P. A., McDonnell, R. A., & Lloyd, C. D. (2015). *Principles of geographical information systems*. Oxford, UK: Oxford University Press.
- Buss, H. L., Brantley, S. L., Scatena, F. N., Bazilevskaya, E. A., Blum, A., Schulz, M., et al. (2013). Probing the deep critical zone beneath the Luquillo Experimental Forest, Puerto Rico. *Earth Surface Processes and Landforms*, 38(10), 1170–1186. <https://doi.org/10.1002/esp.3409>
- Buss, H. L., Sak, P. B., Webb, S. M., & Brantley, S. L. (2008). Weathering of the Rio Blanco quartz diorite, Luquillo Mountains, Puerto Rico: Coupling oxidation, dissolution, and fracturing. *Geochimica et Cosmochimica Acta*, 72(18), 4488–4507. <https://doi.org/10.1016/j.gca.2008.06.020>
- Caine, J. S., & Tomasiak, S. R. (2003). Brittle structures and their role in controlling porosity and permeability in a complex Precambrian crystalline-rock aquifer system in the Colorado Rocky Mountain Front Range. *Geological Society of America Bulletin*, 115(11), 1410–1424. <https://doi.org/10.1130/B25088.1>
- Carey, A. M., & Paige, G. B. (2016). Ecological site-scale hydrologic response in a semiarid rangeland watershed. *Rangeland Ecology & Management*, 69(6), 481–490. <https://doi.org/10.1016/j.rama.2016.06.007>
- Chapin, C. E., & Kelley, S. A. (1997). The Rocky Mountain erosion surface in the Front Range of Colorado. In D. W. Bolyard & S. A. Sonnenberg (Eds.), *Geologic history of the Colorado Front Range* (pp. 1943–3048). Denver, CO: Rocky Mountain Association of Geologists.
- Chorover, J., Kretzschmar, R., Garcia-Pichel, F., & Sparks, D. L. (2007). Soil biogeochemical processes within the critical zone. *Elements*, 3(5), 321–326. <https://doi.org/10.2113/gselements.3.5.321>
- Chorover, J., Troch, P. A., Rasmussen, C., Brooks, P. D., Pelletier, J. D., Breshers, D. D., et al. (2011). How water, carbon, and energy drive critical zone evolution: The Jemez–Santa Catalina Critical Zone Observatory. *Vadose Zone Journal*, 10(3), 884–899. <https://doi.org/10.2136/vzj2010.0132>
- Clarke, B. A., & Burbank, D. W. (2011). Quantifying bedrock-fracture patterns within the shallow subsurface: Implications for rock mass strength, bedrock landslides, and erodibility. *Journal of Geophysical Research*, 116, F04009. <https://doi.org/10.1029/2011JF001987>
- Dethier, D. P., & Lazarus, E. D. (2006). Geomorphic inferences from regolith thickness, chemical denudation and CRN erosion rates near the glacial limit, Boulder Creek catchment and vicinity, Colorado. *Geomorphology*, 75(3–4), 384–399. <https://doi.org/10.1016/j.geomorph.2005.07.029>
- Dethier, D. P., Ouimet, W., Bierman, P. R., Rood, D. H., & Balco, G. (2014). Basins and bedrock: Spatial variation in ¹⁰Be erosion rates and increasing relief in the southern Rocky Mountains, USA. *Geology*, 42(2), 167–170. <https://doi.org/10.1130/G34922.1>
- Dijkstra, E. W. (1959). A note on two problems in connexion with graphs. *Numerische Mathematik*, 1(1), 269–271. <https://doi.org/10.1007/BF01386390>
- Dixon, J. L., Heimsath, A. M., & Amundson, R. (2009). The critical role of climate and saprolite weathering in landscape evolution. *Earth Surface Processes and Landforms*, 34(11), 1507–1521. <https://doi.org/10.1002/esp.1836>
- Dixon, J. L., & Riebe, C. S. (2014). Tracing and pacing soil across slopes. *Elements*, 10(5), 363–368. <https://doi.org/10.2113/gselements.10.5.363>
- Dubrule, O. (1984). Comparing splines and kriging. *Computers & Geosciences*, 10(2–3), 327–338. [https://doi.org/10.1016/0098-3004\(84\)90030-X](https://doi.org/10.1016/0098-3004(84)90030-X)
- Dvorkin, J., Prasad, M., Sakai, A., & Lavoie, D. (1999). Elasticity of marine sediments: Rock physics modeling. *Geophysical Research Letters*, 26, 1,781–1,784. <https://doi.org/10.1029/1999GL900332>
- Edwards, B. R., & Frost, C. D. (2000). An overview of the petrology and geochemistry of the Sherman batholith, southeastern Wyoming. *Rocky Mountain Geology*, 35(1), 113–137. <https://doi.org/10.2113/35.1.113>

- Egglar, D., Larson, E., & Bradley, W. (1969). Granites grusses and the Sherman erosion surface, southern Laramie Range Colorado-Wyoming. *American Journal of Science*, 267(4), 510–522. <https://doi.org/10.2475/ajs.267.4.510>
- Evanoff, E. (1990). Early Oligocene paleovalleys in southern and central Wyoming: Evidence of high local relief on the late Eocene unconformity. *Geology*, 18(5), 443–446. [https://doi.org/10.1130/0091-7613\(1990\)018%3C0443:EOPISA%3E2.3.CO;2](https://doi.org/10.1130/0091-7613(1990)018%3C0443:EOPISA%3E2.3.CO;2)
- Fletcher, R. C., & Brantley, S. L. (2010). Reduction of bedrock blocks as corestones in the weathering profile: Observations and model. *American Journal of Science*, 310(3), 131–164. <https://doi.org/10.2475/03.2010.01>
- Fletcher, R., Buss, H., & Brantley, S. (2006). A spheroidal weathering model coupling porewater chemistry to soil thicknesses during steady-state denudation. *Earth and Planetary Science Letters*, 244(1–2), 444–457. <https://doi.org/10.1016/j.epsl.2006.01.055>
- Frost, C. D., Frost, B. R., Chamberlain, K. R., & Edwards, B. R. (1999). Petrogenesis of the 1.43 Ga Sherman batholith, SE Wyoming, USA: A reduced, rapakivi-type anorogenic granite. *Journal of Petrology*, 40(12), 1771–1802. <https://doi.org/10.1093/ptro/40.12.1771>
- Galipeau, J. M., & Ragland, P. C. (1979). Whole-rock chemical constraints on the origin of the Virginia Dale ring dike complex, Colorado-Wyoming. *Geochemical Journal*, 13(5), 207–216. <https://doi.org/10.2343/geochemj.13.20>
- Garambois, S., Sénéchal, P., & Perroud, H. (2002). On the use of combined geophysical methods to assess water content and water conductivity of near-surface formations. *Journal of Hydrology*, 259(1–4), 32–48. [https://doi.org/10.1016/S0022-1694\(01\)00588-1](https://doi.org/10.1016/S0022-1694(01)00588-1)
- Gburek, W. J., Folmar, G., & Urban, J. B. (1999). Field data and ground water modeling in a layered fractured aquifer. *Ground Water*, 37(2), 175–184. <https://doi.org/10.1111/j.1745-6584.1999.tb00972.x>
- Gburek, W. J., & Urban, J. B. (1990). The shallow weathered fracture layer in the near-stream zone. *Ground Water*, 28(6), 875–883. <https://doi.org/10.1111/j.1745-6584.1990.tb01723.x>
- Geist, D. J., Frost, C. D., Kolker, A., & Frost, B. R. (1989). A geochemical study of magmatism across a major terrane boundary: Sr and Nd isotopes in proterozoic granitoids of the Southern Laramie Range, Wyoming. *The Journal of Geology*, 97(3), 331–342. <https://doi.org/10.1086/629306>
- Ghosh, A., Becker, T. W., & Humphreys, E. D. (2013). Dynamics of the North American continent. *Geophysical Journal International*, 194(2), 651–669. <https://doi.org/10.1093/gji/ggt151>
- Goodfellow, B. W. (2012). A granulometry and secondary mineral fingerprint of chemical weathering in periglacial landscapes and its application to blockfield origins. *Quaternary Science Reviews*, 57, 121–135. <https://doi.org/10.1016/j.quascirev.2012.09.023>
- Goodfellow, B. W., Hilley, G. E., Webb, S. M., Sklar, L. S., Moon, S., & Olson, C. A. (2016). The chemical, mechanical, and hydrological evolution of weathering granitoid: Granite weathering. *Journal of Geophysical Research: Earth Surface*, 121, 1410–1435. <https://doi.org/10.1002/2016JF003822>
- Graham, R., Rossi, A., & Hubbert, R. (2010). Rock to regolith conversion: Producing hospitable substrates for terrestrial ecosystems. *GSA Today*, 4–9. <https://doi.org/10.1130/GSAT57A.1>
- Graham, R. C., Anderson, M. A., Sternberg, P. D., Tice, K. R., & Schoeneberger, P. J. (1997). Morphology, porosity, and hydraulic conductivity of weathered granitic bedrock and overlying soils. *Soil Science Society of America Journal*, 61(2), 516–522. <https://doi.org/10.2136/sssaj1997.03615995006100020021x>
- Gregory, K. M., & Chase, C. G. (1994). Tectonic and climatic significance of a late Eocene low-relief, high-level geomorphic surface, Colorado. *Journal of Geophysical Research*, 99, 20,141–20,160. <https://doi.org/10.1029/94JB00132>
- Hahn, W. J., Riebe, C. S., Lukens, C. E., & Araki, S. (2014). Bedrock composition regulates mountain ecosystems and landscape evolution. *Proceedings of the National Academy of Sciences of the United States of America*, 111(9), 3338–3343. <https://doi.org/10.1073/pnas.1315667111>
- Hayes, J. L. (2016). Seismic refraction studies of volcanic crust in Costa Rica and of critical zones in the southern Sierra Nevada, California and Laramie Range, Wyoming (PhD). University of Wyoming, United States -- Wyoming. Retrieved from <http://search.proquest.com/libproxy.uwyo.edu/pqdlocal1005743/docview/1801725446/abstract/9E567E53B84E7CPQ/4>
- Heimsath, A. M., DiBiase, R. A., & Whipple, K. X. (2012). Soil production limits and the transition to bedrock-dominated landscapes. *Nature Geoscience*, 5(3), 210–214. <https://doi.org/10.1038/ngeo1380>
- Heincke, B., Maurer, H., Green, A. G., Willenberg, H., Spillmann, T., & Burlini, L. (2006). Characterizing an unstable mountain slope using shallow 2D and 3D seismic tomography. *Geophysics*, 71(6), B241–B256. <https://doi.org/10.1190/1.2338823>
- Hilley, G. E., Chamberlain, C. P., Moon, S., Porder, S., & Willett, S. D. (2010). Competition between erosion and reaction kinetics in controlling silicate-weathering rates. *Earth and Planetary Science Letters*, 293(1–2), 191–199. <https://doi.org/10.1016/j.epsl.2010.01.008>
- Holbrook, W. S., Riebe, C. S., Elwaseif, M., Hayes, J. L., Basler-Reeder, K., Harry, D. L., et al. (2014). Geophysical constraints on deep weathering and water storage potential in the Southern Sierra Critical Zone Observatory. *Earth Surface Processes and Landforms*, 39(3), 366–380. <https://doi.org/10.1002/esp.3502>
- Holloway, J. M., Dahlgren, R. A., Hansen, B., & Casey, W. H. (1998). Contribution of bedrock nitrogen to high nitrate concentrations in stream water. *Nature*, 395(6704), 785–788. <https://doi.org/10.1038/27410>
- Hood, J. L., Roy, J. W., & Hayashi, M. (2006). Importance of groundwater in the water balance of an alpine headwater lake. *Geophysical Research Letters*, 33, L13405. <https://doi.org/10.1029/2006GL026611>
- Houston, R. S., & Marlatt, G. (1997). Proterozoic geology of the Granite Village area, Albany and Laramie counties, Wyoming, compared with that of the Sierra Madre and Medicine Bow mountains of southeastern Wyoming (USGS Numbered Series No. 2159). USGS. Retrieved from <http://pubs.er.usgs.gov/publication/b2159>
- Jencso, K. G., McGlynn, B. L., Gooseff, M. N., Bencala, K. E., & Wondzell, S. M. (2010). Hillslope hydrologic connectivity controls riparian groundwater turnover: Implications of catchment structure for riparian buffering and stream water sources. *Water Resources Research*, 46, W10524. <https://doi.org/10.1029/2009WR008818>
- Katsuyama, M., Tani, M., & Nishimoto, S. (2010). Connection between streamwater mean residence time and bedrock groundwater recharge/discharge dynamics in weathered granite catchments. *Hydrological Processes*, 24(16), 2287–2299. <https://doi.org/10.1002/hyp.7741>
- Kollet, S. J., & Maxwell, R. M. (2008). Capturing the influence of groundwater dynamics on land surface processes using an integrated, distributed watershed model. *Water Resources Research*, 44, W02402. <https://doi.org/10.1029/2007WR006004>
- Kuntz, B. W., Rubin, S., Berkowitz, B., & Singha, K. (2011). Quantifying solute transport at the Shale Hills Critical Zone Observatory. *Vadose Zone Journal*, 10(3), 843. <https://doi.org/10.2136/vzj2010.0130>
- Lebedeva, M. I., & Brantley, S. L. (2013). Exploring geochemical controls on weathering and erosion of convex hillslopes: Beyond the empirical regolith production function. *Earth Surface Processes and Landforms*, 38(15), 1793–1807. <https://doi.org/10.1002/esp.3424>
- Lebedeva, M. I., Fletcher, R. C., Balashov, V. N., & Brantley, S. L. (2007). A reactive diffusion model describing transformation of bedrock to saprolite. *Chemical Geology*, 244(3–4), 624–645. <https://doi.org/10.1016/j.chemgeo.2007.07.008>
- Lebedeva, M. I., Fletcher, R. C., & Brantley, S. L. (2010). A mathematical model for steady-state regolith production at constant erosion rate. *Earth Surface Processes and Landforms*, 35(5), 508–524. <https://doi.org/10.1002/esp.1954>

- Leopold, M., Dethier, D., Völkel, J., Raab, T., Rikert, T. C., & Caine, N. (2008). Using geophysical methods to study the shallow subsurface of a sensitive alpine environment, Niwot Ridge, Colorado Front Range, U.S.A. *Arctic, Antarctic, and Alpine Research*, *40*(3), 519–530. [https://doi.org/10.1657/1523-0430\(06-124\)%5BLEOPOLD%5D2.0.CO;2](https://doi.org/10.1657/1523-0430(06-124)%5BLEOPOLD%5D2.0.CO;2)
- Leopold, M., Völkel, J., Huber, J., & Dethier, D. (2013). Subsurface architecture of the Boulder Creek Critical Zone Observatory from electrical resistivity tomography. *Earth Surface Processes and Landforms*, *38*(12), 1417–1431. <https://doi.org/10.1002/esp.3420>
- Lichtner, P. C. (1988). The quasi-stationary state approximation to coupled mass transport and fluid-rock interaction in a porous medium. *Geochimica et Cosmochimica Acta*, *52*(1), 143–165. [https://doi.org/10.1016/0016-7037\(88\)90063-4](https://doi.org/10.1016/0016-7037(88)90063-4)
- Long, J. C. S., Remer, J. S., Wilson, C. R., & Witherspoon, P. A. (1982). Porous media equivalents for networks of discontinuous fractures. *Water Resources Research*, *18*, 645–658. <https://doi.org/10.1029/WR018i003p0645>
- Lowry, C. S., Walker, J. F., Hunt, R. J., & Anderson, M. P. (2007). Identifying spatial variability of groundwater discharge in a wetland stream using a distributed temperature sensor. *Water Resources Research*, *43*, W10408. <https://doi.org/10.1029/2007WR006145>
- Maher, K. (2010). The dependence of chemical weathering rates on fluid residence time. *Earth and Planetary Science Letters*, *294*(1–2), 101–110. <https://doi.org/10.1016/j.epsl.2010.03.010>
- Maher, K., & Chamberlain, C. P. (2014). Hydrologic regulation of chemical weathering and the geologic carbon cycle. *Science*, *343*(6178), 1502–1504. <https://doi.org/10.1126/science.1250770>
- Manning, A. H., & Caine, J. S. (2007). Groundwater noble gas, age, and temperature signatures in an Alpine watershed: Valuable tools in conceptual model development. *Water Resources Research*, *43*, W04404. <https://doi.org/10.1029/2006WR005349>
- Martel, S. J. (2006). Effect of topographic curvature on near-surface stresses and application to sheeting joints. *Geophysical Research Letters*, *33*, L01308. <https://doi.org/10.1029/2005GL024710>
- Martel, S. J. (2011). Mechanics of curved surfaces, with application to surface-parallel cracks. *Geophysical Research Letters*, *38*, L20303. <https://doi.org/10.1029/2011GL049354>
- McClymont, A. F., Roy, J. W., Hayashi, M., Bentley, L. R., Maurer, H., & Langston, G. (2011). Investigating groundwater flow paths within proglacial moraine using multiple geophysical methods. *Journal of Hydrology*, *399*(1–2), 57–69. <https://doi.org/10.1016/j.jhydrol.2010.12.036>
- McDonnell, J. J. (2014). The two water worlds hypothesis: Ecohydrological separation of water between streams and trees? The two water worlds hypothesis. *Wiley Interdisciplinary Reviews: Water*, *1*(4), 323–329. <https://doi.org/10.1002/wat2.1027>
- Mears, B. (1993). Geomorphic history of Wyoming and high-level erosions surfaces. In A. W. Snoke, J. R. Steidtmann, & S. M. Roberts (Eds.), *Geology of Wyoming* (Vol. 2, pp. 608–626). Cheyenne, Wyoming: Wyoming Geological Survey.
- Miller, D. J., & Dunne, T. (1996). Topographic perturbations of regional stresses and consequent bedrock fracturing. *Journal of Geophysical Research*, *101*, 25,523–25,536. <https://doi.org/10.1029/96JB02531>
- Mills, H. H. (1990). Thickness and character of regolith on mountain slopes in the vicinity of Mountain Lake, Virginia, as indicated by seismic refraction, and implications for hillslope evolution. *Geomorphology*, *3*(2), 143–157. [https://doi.org/10.1016/0169-555X\(90\)90042-O](https://doi.org/10.1016/0169-555X(90)90042-O)
- Molnar, P., Anderson, R. S., & Anderson, S. P. (2007). Tectonics, fracturing of rock, and erosion. *Journal of Geophysical Research*, *112*, F03014. <https://doi.org/10.1029/2005JF000433>
- Montgomery, D. R. (2007). Is agriculture eroding civilization's foundation? *GSA Today*, *17*(10), 4. <https://doi.org/10.1130/GSAT01710A.1>
- Montgomery, D. R., Dietrich, W. E., Torres, R., Anderson, S. P., Heffner, J. T., & Loague, K. (1997). Hydrologic response of a steep, unchanneled valley to natural and applied rainfall. *Water Resources Research*, *33*, 91–109. <https://doi.org/10.1029/96WR02985>
- Moon, S., Perron, J. T., Martel, S. J., Holbrook, W. S., & St. Clair, J. (2017). A model of three-dimensional topographic stresses with implications for bedrock fractures, surface processes, and landscape evolution: Three-dimensional topographic stress. *Journal of Geophysical Research: Earth Surface*, *122*, 823–846. <https://doi.org/10.1002/2016JF004155>
- Moore, F. E. (1960). Summary of Cenozoic history, southern Laramie Range, Wyoming and Colorado. In R. J. Weimer & J. D. Haun (Eds.), *Guide to the geology of Colorado* (pp. 217–222). Denver, CO: Rocky Mountain Association of Geologists.
- Moser, T. (1991). Shortest-Path Calculation of Seismic Rays. *Geophysics*, *56*(1), 59–67. <https://doi.org/10.1190/1.1442958>
- Moser, T. J., Nolet, G., & Snieder, R. (1992). Ray bending revisited. *Bulletin of the Seismological Society of America*, *82*(1), 259–288.
- Natural Resources Conservation Service (1988). Soil survey of Albany County area, Wyoming. Retrieved from https://www.nrcs.usda.gov/Internet/FSE_MANUSCRIPTS/wyoming/albanyWY1998/albanyWY1998.pdf, Accessed 12/06/2017.
- Natural Resources Conservation Service (2015). Crow Creek SNOTEL site, United States Department of Agriculture, SNOTEL surveys. Retrieved from <http://wcc.sc.egov.usda.gov/nwcc/site?sitenum=1045>, Accessed 07/15/2017.
- Natural Resources Conservation Service (2017). United States Department of Agriculture. Web Soil Survey. Retrieved from <https://websoil-survey.sc.egov.usda.gov/>, Accessed 07/15/2017.
- Navarre-Stichler, A., Brantley, S. L., & Rother, G. (2015). How porosity increases during incipient weathering of crystalline silicate rocks. *Reviews in Mineralogy and Geochemistry*, *80*(1), 331–354. <https://doi.org/10.2138/rmg.2015.80.10>
- Nur, A., Mavko, G., Dvorkin, J., & Galmudi, D. (1998). Critical porosity: A key to relating physical properties to porosity in rocks. *The Leading Edge*, *17*(3), 357–362. <https://doi.org/10.1190/1.1437977>
- Nur, A., & Simmons, G. (1969). The effect of saturation on velocity in low porosity rocks. *Earth and Planetary Science Letters*, *7*(2), 183–193. [https://doi.org/10.1016/0012-821X\(69\)90035-1](https://doi.org/10.1016/0012-821X(69)90035-1)
- Nyquist, J. E., Doll, W. E., Davis, R. K., & Hopkins, R. A. (1996). Cokriging surface topography and seismic refraction data for bedrock topography. *Journal of Environmental and Engineering Geophysics*, *1*(1), 67–74. <https://doi.org/10.4133/JEEG1.1.67>
- Olona, J., Pulgar, J. A., Fernández-Viejo, G., López-Fernández, C., & González-Cortina, J. M. (2010). Weathering variations in a granitic massif and related geotechnical properties through seismic and electrical resistivity methods. *Near Surface Geophysics*, *8*(1750). <https://doi.org/10.3997/1873-0604.2010043>
- Orlando, J., Comas, X., Hynek, S. A., Buss, H. L., & Brantley, S. L. (2016). Architecture of the deep critical zone in the Río Icaos watershed (Luquillo Critical Zone Observatory, Puerto Rico) inferred from drilling and ground penetrating radar (GPR): Drilling and GPR explore weathering in the Río Icaos LCZO watershed. *Earth Surface Processes and Landforms*, *41*(13), 1826–1840. <https://doi.org/10.1002/esp.3948>
- Parsekian, A. D., Singha, K., Minsley, B. J., Holbrook, W. S., & Slater, L. (2015). Multiscale geophysical imaging of the critical zone: Geophysical imaging of the critical zone. *Reviews of Geophysics*, *53*, 1–26. <https://doi.org/10.1002/2014RG000465>
- Pasquet, S., Bodet, L., Dhemaied, A., Mouhri, A., Vitale, Q., Rejiba, F., et al. (2015). Detecting different water table levels in a shallow aquifer with combined P-, surface and SH-wave surveys: Insights from VP/VS or Poisson's ratios. *Journal of Applied Geophysics*, *113*, 38–50. <https://doi.org/10.1016/j.jappgeo.2014.12.005>
- Pavich, M. J. (1986). Processes and rates of saprolite production and erosion on a foliated granite rock of the Virginia Piedmont. In S. M. Colman & D. P. Deithier (Eds.), *Rates of chemical weathering of rocks and minerals* (pp. 551–590). Orlando, FL: Academic Press.
- Pawlik, L., Phillips, J. D., & Samonil, P. (2016). Roots, rock, and regolith: Biomechanical and biochemical weathering by trees and its impact on hillslopes—A critical literature review. *Earth-Science Reviews*, *159*, 142–159. <https://doi.org/10.1016/j.earscirev.2016.06.002>

- Peterman, Z. E., & Hedge, C. E. (1968). Chronology of Precambrian events in the Front Range, Colorado. *Canadian Journal of Earth Sciences*, 5(3), 749–756. <https://doi.org/10.1139/e68-073>
- Pratt, H. R., Swolfs, H. S., Brace, W. F., Black, A. D., & Handin, J. W. (1977). Elastic and transport properties of an in situ jointed granite. *International Journal of Rock Mechanics and Mining Science and Geomechanics Abstracts*, 14(1), 35–45. [https://doi.org/10.1016/0148-9062\(77\)90560-5](https://doi.org/10.1016/0148-9062(77)90560-5)
- Rempe, D. M., & Dietrich, W. E. (2014). A bottom-up control on fresh-bedrock topography under landscapes. *Proceedings of the National Academy of Sciences of the United States of America*, 111(18), 6576–6581. <https://doi.org/10.1073/pnas.1404763111>
- Rempel, A. W., Marshall, J. A., & Roering, J. J. (2016). Modeling relative frost weathering rates at geomorphic scales. *Earth and Planetary Science Letters*, 453, 87–95. <https://doi.org/10.1016/j.epsl.2016.08.019>
- Remy, N., Boucher, A., & Wu, J. (2009). *Applied Geostatistics with SGeMS: A User's Guide*. Cambridge: Cambridge University Press. <https://doi.org/10.1017/CBO9781139150019>
- Riebe, C. S., & Granger, D. E. (2013). Quantifying effects of deep and near-surface chemical erosion on cosmogenic nuclides in soils, saprolite, and sediment. *Earth Surface Processes and Landforms*, 38(5), 523–533. <https://doi.org/10.1002/esp.3339>
- Riebe, C. S., Hahn, W. J., & Brantley, S. L. (2017). Controls on deep critical zone architecture: A historical review and four testable hypotheses. *Earth Surface Processes and Landforms*, 42(1), 128–156. <https://doi.org/10.1002/esp.4052>
- Roberts, M. F. (1970). Late glacial and postglacial environments in southeastern Wyoming. *Palaeogeography, Palaeoclimatology, Palaeoecology*, 8(1), 5–17. [https://doi.org/10.1016/0031-0182\(70\)90075-1](https://doi.org/10.1016/0031-0182(70)90075-1)
- Robinson, D. A., Campbell, C. S., Hopmans, J. W., Hornbuckle, B. K., Jones, S. B., Knight, R., et al. (2008). Soil moisture measurement for ecological and hydrological watershed-scale observatories: A review. *Vadose Zone Journal*, 7(1), 358. <https://doi.org/10.2136/vzj2007.0143>
- Roering, J. J., Marshall, J., Booth, A. M., Mort, M., & Jin, Q. (2010). Evidence for biotic controls on topography and soil production. *Earth and Planetary Science Letters*, 298(1–2), 183–190. <https://doi.org/10.1016/j.epsl.2010.07.040>
- Ruxton, B. P., & Berry, L. (1957). Weathering of granite and associated erosional features in Hong Kong. *Bulletin of the Geological Society of America*, 68(10), 1263–1291. [https://doi.org/10.1130/0016-7606\(1957\)68%5B1263:WOGAAE%5D2.0.CO;2](https://doi.org/10.1130/0016-7606(1957)68%5B1263:WOGAAE%5D2.0.CO;2)
- Ruxton, V. B. P., & Berry, L. (1959). The basal rock surface on weathered granitic rocks. *Proceedings of the Geologists' Association*, 70(4), 285–290. [https://doi.org/10.1016/S0016-7878\(59\)80010-9](https://doi.org/10.1016/S0016-7878(59)80010-9)
- Scott, G. R., & Taylor, R. B. (1986). *Map showing late Eocene erosion surface, Oligocene-Miocene paleovalleys and Tertiary deposits in the Pueblo, Denver, and Greely 1° x 2° quadrangles, Colorado (Scale 1:2500,000)*. Denver, CO: USGS.
- Singha, K., Li, L., Day-Lewis, F. D., & Regberg, A. B. (2011). Quantifying solute transport processes: Are chemically “conservative” tracers electrically conservative? *Geophysics*, 76(1), F53–F63. <https://doi.org/10.1190/1.3511356>
- Slim, M., Perron, J. T., Martel, S. J., & Singha, K. (2014). Topographic stress and rock fracture: A two-dimensional numerical model for arbitrary topography and preliminary comparison with borehole observations. *Earth Surface Processes and Landforms*, 40(4), 512–529. <https://doi.org/10.1002/esp.3646>
- St. Clair, J. (2015). Geophysical investigations of underplating at the Middle American Trench, weathering in the critical zone, and snow water equivalent in seasonal snow (PhD). University of Wyoming, United States -- Wyoming.
- St. Clair, J. S., Moon, S., Holbrook, W. S., Perron, J. T., Riebe, C. S., Martel, S. J., et al. (2015). Geophysical imaging reveals topographic stress control of bedrock weathering. *Science*, 350(6260), 534–538. <https://doi.org/10.1126/science.aab2210>
- Steeffel, C., Depaolo, D., & Lichtner, P. (2005). Reactive transport modeling: An essential tool and a new research approach for the Earth sciences. *Earth and Planetary Science Letters*, 240(3–4), 539–558. <https://doi.org/10.1016/j.epsl.2005.09.017>
- Toth, J. (1999). Groundwater as a geologic agent: An overview of the causes, processes, and manifestations. *Hydrogeology Journal*, 7(1), 1–14. <https://doi.org/10.1007/s100400050176>
- Ver Ploeg, A. J., & McLaughlin, J. F. (2010). *Preliminary geologic map of the Sherman Mountains West quadrangle, Albany County, Wyoming (sheet 1, scale 1:24,000)*. Laramie, Wyoming: Wyoming State Geological Survey.
- Voltz, T., Gooseff, M., Ward, A. S., Singha, K., Fitzgerald, M., & Wagener, T. (2013). Riparian hydraulic gradient and stream-groundwater exchange dynamics in steep headwater valleys. *Journal of Geophysical Research: Earth Surface*, 118, 953–969. <https://doi.org/10.1002/jgrf.20074>
- Wackernagel, H. (2003). *Multivariate geostatistics: An introduction with applications*. Verlag Berlin Heidelberg and New York: Springer Science & Business Media.
- Walder, J., & Hallet, B. (1985). A theoretical model of the fracture of rock during freezing. *Geological Society of America Bulletin*, 96(3), 336–346. [https://doi.org/10.1130/0016-7606\(1985\)96%3C336:ATMOTF%3E2.0.CO;2](https://doi.org/10.1130/0016-7606(1985)96%3C336:ATMOTF%3E2.0.CO;2)
- White, A. F., Blum, A. E., Schulz, M. S., Vivit, D. V., Stonestrom, D. A., Larsen, M., et al. (1998). Chemical weathering in a tropical watershed, Luquillo mountains, Puerto Rico: I. Long-term versus short-term weathering fluxes. *Geochimica et Cosmochimica Acta*, 62(2), 209–226. [https://doi.org/10.1016/S0016-7037\(97\)00335-9](https://doi.org/10.1016/S0016-7037(97)00335-9)
- White, T., Brantley, S., Banwart, S., Chorover, J., Dietrich, W., Derry, L., et al. (2015). Chapter 2—The role of critical zone observatories in critical zone science. In J. R. Giardino & C. Houser (Eds.), *Developments in Earth Surface Processes* (Vol. 19, pp. 15–78). Amsterdam, Netherlands: Elsevier. <https://doi.org/10.1016/B978-0-444-63369-9.00002-1>
- Zielinski, R. A., Peterman, Z. E., Stuckless, J. S., Rosholt, J. N., & Nkomo, I. T. (1982). The chemical and isotopic record of rock-water interaction in the Sherman granite, Wyoming and Colorado. *Contributions to Mineralogy and Petrology*, 78(3), 209–219. <https://doi.org/10.1007/BF00398915>